FLOOD-FREEZE CYCLES AND MICROALGAL DYNAMICS IN ANTARCTIC PACK ICE

Christian H. Fritsen[1], Stephen F. Ackley[2], James N. Kremer[3], and Cornelius W. Sullivan[4]

Dynamics of surface and bottom-ice microalgal communities were investigated using a numerical model of ice growth, ice hydrostatics, radiative transfer processes, nutrient exchange processes, and microalgal growth. Annual simulations showed a general succession of ice properties and microalgal dynamics related to flood-freeze cycles. Specifically, microalgal blooms were predicted to accumulate on the bottom of first-year ice during the austral autumn when ice was actively thickening yet thin enough to allow sufficient light penetration for algal growth. During the austral spring, simulations showed flooding of seawater onto the surface of the ice due to snow loading, which resulted in algal blooms in the flooded snow. In ice that survived a summer melting season, the model predicted an additional growth of surface algae during the autumnal period when the flooded snow froze. During subsequent spring-summer periods, little or no growth or accumulation of algae was predicted at the bottom of the ice due to frequent ice ablation and a predominantly low-light environment. Sensitivity analyses showed that variations in ocean heat flux, snow fall, and atmospheric temperature determined the timing and location of the predicted algal blooms in sea ice. These general findings are consistent with field observations, and may explain the processes responsible for observed differences between algal distributions and dynamics in different oceanic settings.

INTRODUCTION

Within Antarctic pack ice, microalgal communities proliferate in a variety of sea ice habitats [*Horner et. al*, 1992]. Biomass produced within these sea-ice habitats provides an important energy supply for the Antarctic marine ecosystem and its principle components [e.g., *El-Sayed*, 1984; *Kottmeier and Sullivan*, 1990; *Daly*, 1990; *Franeker*, 1994].

Sea ice habitats are (by convention) designated by their position within the sea ice and are generally categorized as surface, interior or bottom-ice [*Horner et al.*, 1992]. Within each of these general categories, additional descriptive habitat designations are often used, and are based on additional characteristics such as mode of formation or location relative to some other geophysical feature of the sea ice. For instance, melt pools and deformation ponds are types of surface habitats that are designated by their mode of formation.

Investigations of seasonal dynamics in geophysical properties of sea ice habitats and distributions of ice biota have been focused primarily in coastal regions near land-based research stations where fast-ice predominates and bottom-ice communities prevail [e.g., *Bunt*, 1963; *Sullivan et al.*, 1985; *Grossi et al.*, 1987; *Arrigo et al.*, 1995]. Experiments comparable to those that have occurred near land-based research stations are lacking in the more extensive pack ice regime where surface and interior ice-algal communities appear to be

[1]Department of Biology, Montana State University, Bozeman, Montana

[2]Cold Regions Research and Engineering Laboratory, Army Corp of Engineers, Hanover, New Hampshire

[3]Department of Marine Sciences, Avery Point Campus, University of Connecticut, Groton, Connecticut

[4]Department of Biological Sciences, University of Southern California, Los Angeles, California

predominant [e.g., *Garrison et al.*, 1986; *Garrison and Buck*, 1991; *Ackley and Sullivan*, 1994].

Beyond a general knowledge of microalgal habitats found in Antarctic sea ice [*Garrison et al.*, 1986; *Ackley and Sullivan*, 1994], relatively little is known regarding the distribution and quantitative importance of the environmental factors governing (1) creation of surface habitats, (2) establishment of associated microbial communities, and (3) microalgal growth within these habitats over the broad range of oceanographic settings around Antarctica. Therefore we developed a numerical model to investigate the environmental factors that determine the time-varying geophysical properties of sea ice as they relate to (1) creation of surface as well as bottom-ice habitat, and (2) the dynamics of both surface and bottom-ice microalgal communities. Our numerical model was developed using previous formulations of ice thermodynamics [e.g., *Maykut and Untersteiner*, 1971] and microalgal growth in land-fast ice [*Arrigo et al.*, 1993] with additional algorithms that allow for snow-induced flood-freeze cycles (which are driven primarily by variations in snowfall, ocean heat fluxes, and atmospheric temperatures). We used this model as an analytical tool to investigate the processes governing microalgal dynamics in the surface and bottom-ice habitats under a variety of oceanographic and meteorologic settings that occur in the ice-covered Southern Ocean.

MODEL DESCRIPTION

Ice Growth

Ice growth formulations are modified versions of previous works describing ice growth via thermodynamic losses of heat from the lower ice boundary [*Stefan*, 1891; *Maykut and Untersteiner*, 1971]. The equations determining rates of ice growth are outlined briefly in the following paragraphs. Specific details regarding the fundamental equations and coefficients are presented elsewhere [*Maykut and Untersteiner*, 1971; *Maykut*, 1986]. Variables and notations are presented in Table 1.

The rate of ice thickening due to freezing at the bottom of the ice sheet (dH_i/dt) is related to the balance of the heat fluxes at the lower ice interface such that

$$\frac{dH_i}{dt} = -\frac{1}{\rho_i L_f}(F_c + F_w) \qquad (1)$$

[*Maykut*, 1986], where L_f is the latent heat of fusion, ρ_i

is the ice density, F_w is the heat flux from the water column, and F_c is the conductive heat loss from the lower ice interface. F_w is influenced by mixed layer dynamics [e.g., *McPhee and Martinson*, 1994] and radiation inputs into the mixed layer [*Maykut and Perovich*, 1987]. In the present model, F_w either is set and assumed constant or can be a time-varying input into the model.

F_c was determined by the thermal conductance of the combined ice and snow (k_{i+s}), and the thermal gradient in the ice as

$$F_c = k_{i+s}\frac{T_0 - T_f}{H_i} \qquad (2)$$

where T_f is the freezing temperature of seawater, k_{i+s} is given as

$$k_{i+s} = \frac{k_i k_s}{k_i h_s + k_s H_i} \qquad (3)$$

and T_0 is the temperature at the upper surface of the ice (or snow, when present). T_0 was determined by the net losses or gains of energy at the surface boundary. A solution for T_0 was provided by *Maykut* [1986] as

$$T_0 = \frac{C_t T_a - k_{i+s} T_f}{C_t + k_{i+s}} \qquad (4)$$

where C_t is a bulk heat-transport term that combines the transport of sensible and latent heat. The thermal conductivity of the snow was formulated based on its density, whereas the thermal conductivity of the sea ice was determined from temperature and salinity [*Maykut and Untersteiner*, 1971].

Initial pancake-ice formation and ice-deformation processes were not explicitly modeled; an initial ice thickness was set by the user. In general, the initial ice thickness should be set at ≥ 20 to 30 cm, above which thermodynamic growth should start to predominate.

Hydrostatic Balance, Flooding, and Freezing

A flood-freeze algorithm was developed by combining mathematical descriptions of ice growth and hydrostatics. Flooding of the surface of the sea ice with seawater can only occur when two criteria are met. First, the ice freeboard height (H_{fb}, the distance be-

TABLE 1. Model Notation and Units.

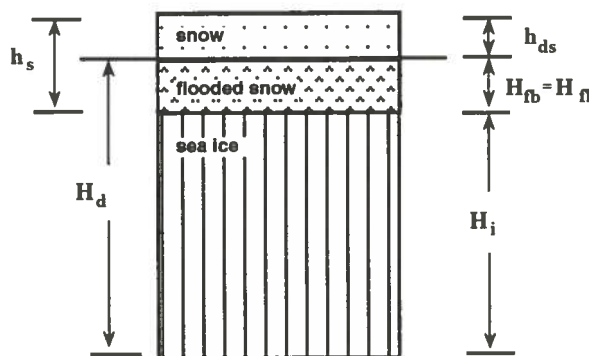| Variable	Description	Unit
$a*$	pigment specific absorption coefficient	m^2 mg chla^{-1}
a_d	diffuse absorption coefficient	m^{-1}
b_b	backscattering coefficient	m^{-1}
C_{alg}	concentration of algae	mg chl$a$ m^{-3}
C_t	bulk heat transport coefficient	W m^{-2} $°C^{-1}$
D	nutrient dilution rate	h^{-1}
E_d	downwelling irradiance	μE m^{-2} s^{-1}
E_u	upwelling irradiance	μE m^{-2} s^{-1}
E_o	scalar irradiance	μE m^{-2} s^{-1}
E_{od}	downwelling scalar irradiance	μE m^{-2} s^{-1}
E_{ou}	upwelling scalar irradiance	μE m^{-2} s^{-1}
F_{br}	volume flux of brine	m^3 m^{-2} h^{-1}
F_c	internal heat conduction	W m^{-2}
F_w	oceanic heat flux	W m^{-2}
g	specific algal loss rate due to grazing	h^{-1}
H_i	ice thickness	m
H_d	ice draft	m
H_{df}	draft of flooded ice	m
H_{fb}	freeboard thickness	m
H_{ff}	depth of freezing front	m
h_{ds}	thickness of dry snow	m
h_s	snow thickness (both dry and flooded)	m
K	irradiance diffuse attenuation coefficient	m^{-1}
K_s	half-saturation constant for N_i uptake	μM
k_i	thermal conductivity of sea ice	W m^{-1} $°C^{-1}$
k_s	thermal conductivity of snow	W m^{-1} $°C^{-1}$
L_f	latent heat of freezing	joules kg^{-1}
L_{lim}	light limitation	unitless
N_{br}	nutrient concentration in the brine	μM
N_{sw}	nutrient concentration in seawater	μM
N_{lim}	nutrient limitation term	unitless
PUR	photosynthetically usable radiation	μE m^{-2} s^{-1}
R	irradiance reflectance	unitless
R_{lim}	resource limitation	unitless
S_{lim}	salinity limitation	unitless
S_b	brine salinity	psu
T_a	atmospheric temperature	°C
T_f	freezing temperature of seawater	°C
T_o	surface temperature	°C
V_b	fractional brine volume	unitless
z	depth	m
μ	specific algal growth rate	hr^{-1}
μ_d	mean-cosine downwelling radiance	unitless
μ_d	mean-cosine upwelling radiance	unitless
μ_{max}	maximum specific algal growth rate	h^{-1}
Π	porosity	unitless
ρ_{fl}	density of flooded ice	g cm^{-3}
ρ_{ice}	sea ice density	g cm^{-3}
ρ'_i	pure ice density	g cm^{-3}
ρ_s	snow density	g cm^{-3}
ρ_{sw}	density of seawater	g cm^{-3}

Fig. 1. Cross-section of an ice sheet showing the vertical dimensions and notation used to describe the different layers within the sea ice and snow (terms are listed in Table 1 and explained in the text).

tween the ice surface and sea level) has to be negative, and second, there have to be conduits for water to infiltrate to the ice surface.

Freeboard height, which is determined by the hydrostatics of the ice cover, was modeled according to Archimedes' principle (buoyancy force is proportional to the displacement volume). Assuming that the volume of a submerged object is the volume of displaced fluid, then the draft of the sea ice (the distance from sea level to the bottom of the ice, H_d) was calculated as

$$H_d = \frac{H_i \, \rho_i + h_s \, \rho_s}{\rho_{sw}} \qquad (5).$$

Freeboard height is then the difference between the draft and the ice thickness.

When freeboard height becomes negative the ice has the potential to flood, but will flood only when the ice and snow are permeable to seawater. Infiltration of seawater onto the surface of the ice can be modeled from either of two heuristic approaches. First, cracks in the ice and or lateral infiltration are always potential passageways for flooding any time the freeboard height is negative. Second, according to *Cox and Weeks* [1988], brine channels near the lower boundary of actively growing sea ice become restricted and closed when brine fractions are less than 70 ppt. Using this observation as a first-order estimate of permeability, we assumed that brine fractions in the ice have to be larger than 70 ppt in order for the ice to flood from below. Brine fractions were predicted according to the equations of *Cox and Weeks* [1988], which are temperature and salinity dependent.

Salinity profiles of ice cores from Antarctic seas do not conform to salinity distributions predicted from conventional ice growth and desalination models [*Eicken*, 1992]. Because mechanistic models that predict salinity distributions in the pack ice do not (to our knowledge) exist, we assumed that once sea ice is formed it has a constant salinity of 8 psu. The temperature at which sea ice with salinity of 8 psu has brine fractions greater than 70 ppt is -6°C; this defined our default critical ice temperature at which conduits were presumed to be open and surface flooding would occur. The critical flooding temperature is a variable that can be changed in each model run.

Once the ice floods, the assumption that the volume of displaced water is equal to the volume of the sea ice below sea level is no longer valid, and the draft of the ice has to be adjusted to account for the infiltration of the seawater into the snow and ice. Assuming that wicking of seawater into the snow cover above sea level does not substantially affect the hydrostatic balance, then the draft of a flooded floe (H_{df}) was calculated as

$$H_{df} = \frac{H_i \, \rho_i}{\rho_{sw}} \left[2 - \frac{\rho_{fl}}{\rho'_i} \right] + \frac{h_s \, \rho_s}{\rho_{sw}} \left[2 - \frac{\rho_s}{\rho'_i} \right] \qquad (6)$$

where ρ'_i is the density of pure ice, and ρ_{fl} is the density of sea ice in the flooded state. This equation simply increases the draft in proportion to the volume of water that infiltrates the snow and permeable ice. The depth of flooding on the surface of the ice, H_{fl}, is the freeboard of the ice when in the flooded condition. The depth of the dry snow, h_{ds}, is the snow thickness minus the depth of flooding (Figure 1).

Coupling Algorithms for Ice Growth and Hydrostatic Balance

The logic of combining the algorithms for hydrostatic balance and ice growth is straightforward until freeboard heights become negative. The ice growth model was initiated from initial conditions set by the user. At each time step, dH_i/dt was calculated and added onto the existing H_i. Concurrently, h_s was updated and H_{fb} was determined. If H_{fb} was positive then the loop began again with the appropriate forcing functions for the specified t.

When freeboard height became negative, flooding was allowed to occur if certain criteria were met. Specifically, there had to be conduits allowing the

infiltration of seawater into the snow. If conduits were present, then flooding was allowed. At this point, two separate thermodynamic algorithms were employed. One simulated the lower boundary; the other simulated the freezing of seawater within the flooded snow and ice. First, the lower boundary was simulated according to Equation 1. Temperature gradients in the sea ice below the flooding seawater were assumed to be zero, and F_c was set accordingly to zero. Therefore, ice thickness remained constant if F_w was zero; otherwise, ablation from the bottom occurred at a rate determined by F_w. Second, a modified ice growth equation was used to propagate freezing fronts through flooded snow and the underlying sea ice. The formulation was Stefan's general thermodynamic equation (Equation 1) with a porosity term (Π_x) added to account for the ice crystals already present below the freezing front

$$\frac{dH_{ff}}{dt} = -\frac{1}{\Pi_x \, \rho_i \, L_f} \, (F_c + F_w) \qquad (7)$$

[Lepparanta, 1993], where dH_{ff}/dt is the change in the position of the freezing front and Π_x is the porosity of either snow (x = snw) or ice (x = ice) depending on the position of H_{ff} at time, t.

When the freezing front reached the bottom of the sea ice, the ice was no longer considered to be in a transient flooded condition. Ice that grew in the flooded snow layer was added to the sea ice thickness. The algorithm for propagating freezing fronts was then bypassed and the general algorithm for ice growth (Equation 1) was used to determine dH_i/dt.

Radiative Transfer

The diffuse and direct irradiances [as a function of wavelength (λ)] that reach the surface of the ice and snow were predicted on the basis of latitude, day of the year, and time of the day. The algorithms used were described previously by *Brine and Iqbal* [1983] as utilized by *Arrigo et al.* [1992]. This formulation accounts for variability in transmissivity due to atmospheric aerosols, ozone, and water vapor and is corrected for cloud cover according to *Sverdrup et al.* [1947].

The incident irradiances, direct and diffuse, that were predicted from the atmospheric radiative transfer algorithms were reflected differentially from the snow interface. When snow was not present, specular reflec-

tion of the diffuse component of irradiance was assumed to be 0.05 of the incident value while the direct component was reflected as a function of sun angle. When snow was present (the general case for Antarctic sea ice), both the direct and diffuse components of specular reflection were assumed to be 0.05 of the incident value [*Grenfell*, 1991]. Except in regions where wind scouring of the ice occurs, snow and/or frost flowers (which are optically more similar to snow than ice) are almost always present on ice which is more than a few days old [*Allison*, 1989; Fritsen, personal observation].

Downwelling irradiances, $E_d(\lambda)$, and upwelling irradiances, $E_u(\lambda)$, in the multi-layered pack ice system were modeled using a two-stream approximation of the radiative transfer equation as described by *Schlatter* [1972]. Briefly, downwelling and upwelling irradiances at depth (z) were given as

$$E_d(\lambda, z) = E_d(\lambda, z) \exp[-K(\lambda, z) \, z] \qquad (8)$$

and

$$E_u(\lambda, z) = R(\lambda) \, E_d(\lambda, z) \exp[-K(\lambda, z) \, z] \qquad (9)$$

where $R(\lambda)$ is the ratio of the upward to downward flux of radiation with wavelength, λ, and was defined as

$$R(\lambda) = [a_d(\lambda) + b_b(\lambda) - K(\lambda)] \, b_b(\lambda)^{-1} \qquad (10)$$

where $a_d(\lambda)$ is the diffuse absorption coefficient, $b_b(\lambda)$ is the backscattering coefficient, and $K(\lambda)$ is the total attenuation coefficient, which was defined as

$$K(\lambda) = (a_d^2 + 2 \, a_d \, b_b)^{0.5} \qquad (11)$$

[*Schlatter*, 1972; *Perovich*, 1990]. Note that $K(\lambda)$, as well as $a_d(\lambda)$ and $b_b(\lambda)$, in the two-stream approximation are apparent and quasi-inherent optical properties, and they depend on the radiance distribution [*sensu Kirk*, 1983]. These terms should not be confused with the inherent optical properties of absorption (a), scattering (b), and beam attenuation (c). Backscattering coefficients estimated for different types of snow and sea ice [*Perovich*, 1990] were used in the model.

The diffuse absorption coefficient (a_d) was approximated from the inherent absorption coefficient (a) by invoking the relationship between the inherent properties and quasi-inherent coefficient according to

$$a_d = a \, \mu_{d-1} \qquad (12)$$

[Stavn and Weidmann, 1989; Mobley, 1994]. Because these two-flow equations were derived specifically for the case of isotropic radiance distributions for the upwelling and downwelling streams, the mean cosine of the downwelling and upwelling radiance distributions, μ_d and μ_u, are equal to 0.5. The absorption coefficient, a, for each layer of ice or snow was defined as the sum of the absorption coefficients of the ice and the algae within each layer. Absorption coefficients of ice and snow were assumed to be those of polycrystalline ice [Grenfell and Perovich, 1981] while the absorption coefficients of algae were calculated by multiplying the chlorophyll-a-specific absorption coefficient, a^*, by the chlorophyll a concentration within a layer. Chlorophyll-a-specific absorption coefficients for pack ice algae [Fritsen et al., 1992] were used to define a^*.

Downwelling and upwelling irradiances were used to calculate scalar irradiances at depth, $E_o(z)$, from the relationships

$$E_o(z) = E_{od}(z) + E_{ou}(z) \qquad (13)$$

and

$$E_{od}(z) + E_{ou}(z) = E_d(z) \, \mu_{d-1} + E_u(z) \, \mu_{u-1} \qquad (14)$$

[Kirk, 1983]. At the bottom of the ice, E_u was assumed to be negligible [Perovich, 1990; Grenfell, 1991] and $E_o(z)$ was determined by the downwelling irradiances alone.

Algal Growth

Changes in microalgal concentrations, C_{alg}, in the sea ice habitats were formulated as functions of their accumulation due to growth and their losses due to grazing and/or losses due to physical processes such that

$$\frac{dC_{alg}}{dt} = (\mu - g)C_{alg} - P \qquad (15)$$

The specific algal growth rate, μ, was formulated based on the theory of resource limitation and environmental constraints such that

$$\mu = \mu_{max} \, R_{lim} \, S_{lim} \qquad (16)$$

where μ and μ_{max} (hr^{-1}) are the realized and maximum specific growth rates, R_{lim} (dimensionless) is the fractional reduction of μ_{max} due to a resource limitation, and S_{lim} (dimensionless) is a fractional reduction of μ_{max} due to salinity constraints [Arrigo et al., 1993].

Temperature was used to define the maximum possible growth rate, μ_{max} [Eppley, 1972]. Arrigo and Sullivan [1994] reported that this approach at temperatures less than 0°C is reasonable when salinity is not a confounding factor and salinity and temperature effects on algal growth are modeled as multiplicative limiting factors [Arrigo and Sullivan, 1992].

Resources that potentially are limiting to algal growth are either light or nutrients. Nutrient limitation was calculated according to the Monod formulation for microbial growth rates as a function of substrate concentration (N_{br}) such that

$$N_{lim} = \frac{\mu}{\mu_{max}} = \frac{N_{br}}{K_s + N_{br}} \qquad (17)$$

where N_{br} was the nutrient (e.g., nitrate, silicate, or phosphate) concentration in the brine, and K_s was the concentration of the substrate where μ was half of μ_{max}. Any nutrient could be used in this modeling scenario, as long as appropriate coefficients and concentrations are utilized. For the current analysis, the model was run as a nitrate-based model. Nutrient regenerative processes in sea ice habitats are poorly constrained at present and are not accounted for in the present formulation; therefore, the model should be considered as a model of net algal growth and "new" production [sensu Dugdale and Goering, 1967].

Light limitation was predicted based on photosynthetically usable radiation [PUR; Morel, 1978] and I_k' (the flux of photosynthetically usable radiation at which light was no longer limiting; Arrigo et al., 1993] using a rectilinear function

$$L_{lim} = \frac{\mu}{\mu_{max}} = \frac{PUR}{I_k'} \qquad (18)$$

when PUR $< I_k'$, and $L_{lim} = 1$ when PUR $\geq I_k'$. The I_k' parameter describes a photophysiological response of algae; it often coincides with the irradiances at which the algal species are growing. Hence, I_k' is believed to respond to prior exposures to environmental conditions that are integrated over some prior period of time. The time period over which I_k' responds is not well defined

by experimentation. In several modeling studies, photoacclimation was assumed to vary according to environmental conditions over the previous several days [*Kremer and Nixon*, 1978; *Arrigo et al.*, 1993, *Arrigo and Sullivan*, 1994]. Therefore, to be consistent with prior studies, I_k' was assumed to be a function of the PUR over the prior 72 h [*Arrigo and Sullivan*, 1994].

Bottom algae. Microalgal communities grow and accumulate near the ice/seawater interface of actively growing congelation ice and remain near the ice-seawater interface even when ice grows over several decimeters [*Hoshiai*, 1977; *Grossi and Sullivan*, 1985; *Ackley et al.*, 1996; *Fritsen and Sullivan*, in press]. The processes that maintains microalgal populations near the advancing ice/water interface are not understood well. However, this phenomena has been documented on several occasions in several regions of the polar oceans [also in the Arctic; M. Gosselin personal communication]. Therefore, the model was formulated such that a bottom-ice microalgal population in the lower centimeters of the sea ice will maintain its position relative to a growing ice/seawater interface. The bottom-ice algae were assumed to be sloughed into the water column whenever ablation occurred at the lower ice/seawater interface.

Salinity of the brine (S_b) within the bottom ice-algal layer is controlled by ambient temperatures in an ice-seawater solution maintained at phase equilibrium [*Assur*, 1958]. The equations that we used to determine S_b follow from those used by *Cox and Weeks* [1983], which are best-fit polynomial regressions of Assur's original laboratory data. The average S_b of the bottom-ice algal layer was calculated from the temperature in the bottom-ice layer.

Macronutrients were determined by (1) the initial conditions, (2) rates of utilization and remineralization within the system, and (3) rates of import and export. In the bottom layers of actively thickening sea ice, convective brine exchanges with the underlying seawater are thought to drive the flux of nutrients into and out of the ice [*Reeburgh*, 1984]. Therefore, nutrient transports in the bottom-ice were modeled according to the assumptions of *Arrigo et al.* [1992] for nutrient exchanges as a function of brine expulsion that were correlated to the rate of ice growth. The specific formulation for exchange rates in the bottom of the ice were determined by the rate of brine flux (F_{br}, based on best-fit polynomial regressions of original data from *Wakasutchi and Ono* [1983] as published by *Arrigo et al.* [1992]), and the total volume of brine in the lower regions of the ice ($V_b Z_{alg}$) such that the nutrient dilution rate (D) was defined as

$$D = F_{br} (V_b Z_{alg})^{-1} \qquad (19)$$

where V_b was the fractional volume of brine in the layer as determined by salinity and temperature [*Cox and Weeks*, 1988], and Z_{alg} was the thickness of the layer of algae in the bottom of the ice. The thickness of the algal layer near the ice/seawater interface was a variable set at the beginning of each run. To be consistent with previous modeling studies [*Arrigo et al.*, 1993; *Arrigo and Sullivan*, 1994], the default thickness of the bottom-ice algal layer was set at 2 cm.

Changes in nutrient concentrations in the ice were given as the balance of uptake and dilution

$$\frac{dN_{br}}{dt} = D (N_{sw} - N_{br}) - \mu C_{alg} \qquad (20)$$

where ($N_{sw}-N_{br}$) was the difference in the concentrations of nutrient in the seawater (N_{sw}) and the brine (N_{br}).

Surface algae. Several basic assumptions were made in order to model surface communities. First, surface communities were assumed to be located at the ice/snow interface. Second, we assumed that surface communities were incorporated into the interior of the ice once a freeze-flood cycle was completed. Further growth and/or dynamics of the internalized surface communities were not modeled at present. Rather, the algae were incorporated into the ice matrix, and biomass only accumulated through physical incorporation. Below, we will present an analysis of the shortcomings of these assumptions regarding interior communities.

These simplifying assumptions (regarding the location of the surface assemblage in relation to the ice structure) allowed us to simulate the environmental conditions within the surface habitat. The simulated environmental conditions were derived from the same first principles that followed from the physical models outlined above. For instance, temperatures at the surface of the ice were inferred from interpolations of dT/dz through the snow to the ice surface. However, if the sea ice was flooded and the surface of the ice was below the freezing front, then temperatures were set at -1.89°C. When freezing fronts propagate into the snow or ice, salts are rejected from the growing ice matrix; density inversions in the brine can then be created which can lead to convective processes [*Fritsen et al.*,

1994; *Lytle and Ackley*, 1996]. Therefore, we assumed that nutrient exchanges in the surface habitat occurred only when freezing fronts were progressing through the snow [*Fritsen et al.*, 1994]. The dilution rate followed from Equation 19, with D being determined by the porosity of the snow and the depth of the porous layer, and F_{br} predicted by dH_{ff}/dt. Once a freezing front progressed past the location of the surface algae, nutrient exchanges were assumed to stop.

RESULTS AND DISCUSSION

To utilize the model for investigations of sea ice dynamics and to gain insights into processes controlling the dynamics of pack ice microalgal communities, it was necessary to investigate the performance and sensitivity of the model to both assumptions within the model and to the forcing functions and internal coefficients that may be poorly understood or poorly constrained. Because the model was derived from previous models of ice growth [*Maykut and Untersteiner*, 1971], radiative transfer [*Schlatter*, 1972; *Brine and Iqbal*, 1983; *Perovich*, 1990], and algal growth in congelation and platelet ice [*Arrigo et al.*, 1993] analyses were restricted to scenarios with variables, coefficients, and/ or assumptions that are pertinent to flood-freeze cycles and annual to biannual predictions of growth in surface and bottom-ice microalgal communities.

Flood-freeze Dynamics

Once an ice sheet floods and seawater infiltrates the snow, freezing fronts may propagate through the snow/seawater mixture at a rate determined by the heat flux through the snow cover. When atmospheric temperatures are sufficiently cold, freezing fronts propagate into the underlying ice and eventually reach the lower ice surface [*Fritsen et al.*, 1994; *Lytle and Ackley*, 1996]. The dynamics of this process determine the physical and chemical microenvironments within the ice habitats. Therefore, it was necessary to evaluate the model's performance and predictions of the geophysical dynamics during flood-freeze cycles.

During studies in the western Weddell Sea (Ice Station Weddell-1: ISW-1), profiles of temperatures from above the snow, through the ice, and into the water column were recorded on an hourly basis from February to June of 1992 [*Fritsen et al.*, 1994; *Lytle and Ackley*, 1996]. These temperature records, in conjunction with records of ice properties, provided a data set at sufficient time and vertical spacings for evaluating our modeled simulations of flood-freeze cycles.

Two of the sites from ISW-1 (Sites A and B) were utilized to evaluate the model predictions. Site A was located in second-year deformed ice having variable ice and snow thicknesses; some parts of the floe, including the area where the thermistor string was located, had
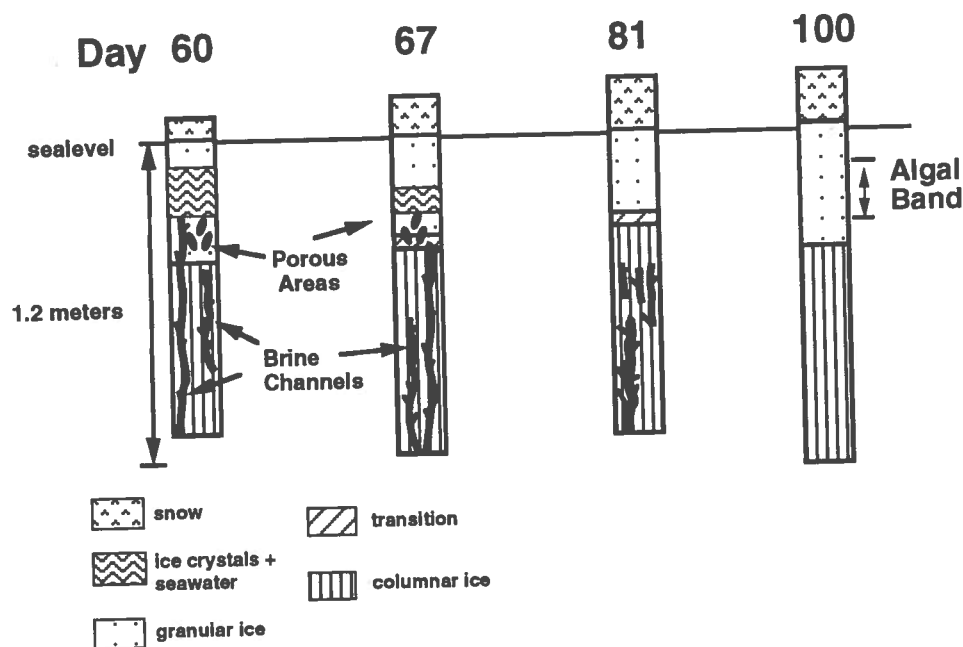

Fig. 2. Morphologies and crystal stratigraphies of sea ice cores obtained at Site B, Ice Station Weddell-1, in 1992.
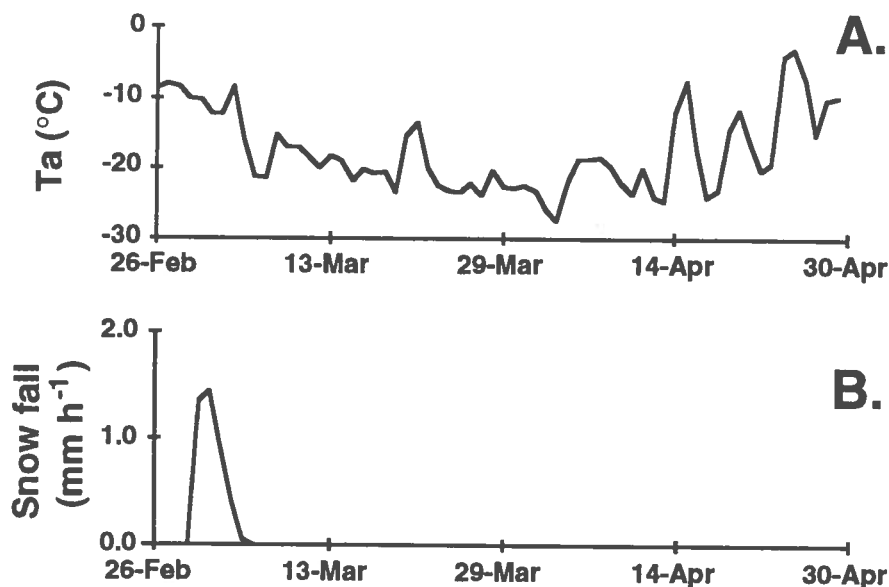
Fig. 3. (a) Atmospheric temperatures recorded at Ice Station Weddell-1 (ISW-1). (b) Rates of snowfall used in simulating freezing front dynamics in second-year ice at ISW-1.

negative freeboard heights that were typically flooded with seawater. The original snow thickness at the location of the thermistors was 40 cm (on February 26) and the ice thickness was 110 cm [*Lytle and Ackley*, 1996]. Site B was located in relatively flat, second-year ice. The thickness of the ice on March 1 was 120 cm with 17 cm of snow. However, the vertical structure of the ice profile (Figure 2) included a 5- to 10-cm layer of consolidated granular ice above a 10-cm layer of unconsolidated ice crystals in seawater. Temperature gradients had been established through the snow at this time [V. Lytle, personal communication]. Therefore, the upper 5 to 10 cm of granular ice is thought to have arisen via freezing of a seawater/snow mixture. Assuming that the upper 5 to 10 cm of surface granular ice arose via freezing of a surface flooded layer, then the original sea ice thickness would have been 85 cm and the snow cover would have been 35 cm before the surface-flood seawater began to freeze.

Simulations of the flooding and freezing dynamics at Sites A and B were undertaken using these initial ice and snow thicknesses and forcings of atmospheric temperatures and snowfall shown in Figure 3a and 3b. The ocean heat flux was held constant at 7 W m^{-2} [*Lytle and Ackley*, 1996], while the density of the snow was held constant at 0.4 g cm^{-3} and the density of the flooded sea ice was set at 0.8 g cm^{-3} based on measurements of the snow and ice properties at these sites [V. Lytle, S. Ackley and C. Fritsen, unpublished data].

Simulation of Site B showed that the snow would have been flooded to depth of 24 cm and a freezing front would have progressed through the flooded layer by March 13 (Figure 4). From March 13 to 25, the model predicted that the freezing front propagated through the ice to the ice-seawater interface. Furthermore, the simulation showed net ice growth occurring at this time and the predicted ice thickness on April 26 was 120 cm. The actual depths of the freezing front inferred from the temperature records at site B are in general agreement with our simulation results for the depths of freezing front progression (Figure 4). The measured ice thickness of 117 cm at Site B on March 31 also compares favorably with the predicted ice
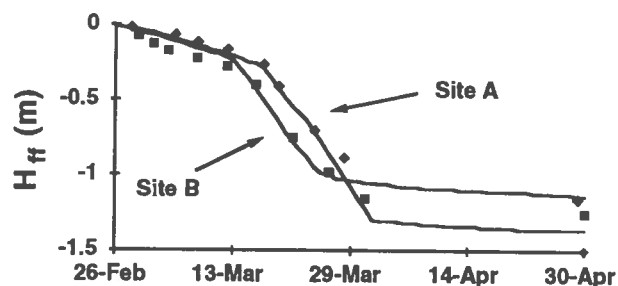

Fig. 4. Simulated (lines) and observed (symbols) changes in the depth of the freezing fronts (Hff) at Sites A (diamonds) and B (circles). The observed positions of the freezing fronts were inferred from thermistor records [*Fritsen et al.*, 1994; *Lytle and Ackley*, 1996].
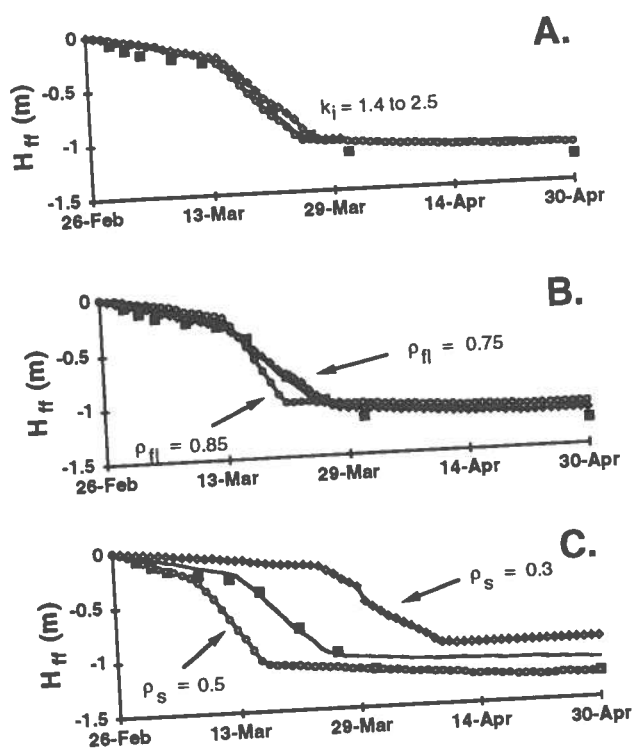
Fig. 5. Sensitivity of the simulated freezing front dynamics to variations in: (a) thermal conductivity of the sea ice, (k_i); (b) density of the flooded sea ice (ρ_{fl}); and (c) the density of the snow, ρ_s. Range of variables: k_i = 1.4 to 2.46 W m^{-1} °C^{-1}; ρ_{fl} = 0.75 to 0.85 g cm^{-3}; ρ_s = 0.3 to 0.5 g cm^{-3}.

thickness of 120 cm. The difference between the simulated and the observed depths of the freezing fronts averaged only 3 cm throughout the timecourse.

At Site A, the freezing front was predicted to progress through the surface flooded layer by March 17 and then to the bottom of the sea ice by April 1 (Figure 4); the slower progression of the freezing front at this site was caused by the thicker, insulating snow cover. Net ice growth after the freezing front reached the bottom of the ice also was predicted for this simulation, which resulted in an ice thickness of 136 cm on April 26. Depths of the freezing front inferred from the thermistors at Site A also agree with the features of our simulated freezing front progression (Figure 4). Unfortunately, the variable thicknesses of the cores taken at Site A provide little evidence for net ice growth at this location. However, dendritic ice (an indicator of new congelation ice growth) was found at the bottom of a 115-cm ice core at Site A in on April 28; this indicates that net ice growth was occurring at this site, and that our prediction of net ice growth for this site is reasonable.

Snow density, density of the flooded ice, and the thermal conductivity of the sea ice are variables directly affecting the simulation of ice thermodynamics during flood-freeze cycles; therefore, uncertainties in these variables may limit our model's ability to accurately predict these processes. Varying the thermal conductivity of the sea ice from 1.40 to 2.46 W m^{-1} °C^{-1} (corresponding to a range in ice salinities of 5 to 10 ppt and ice temperatures of -1.89 to -30°C) produced simulations that predicted the freezing front progression through the flooded snow at Site B would vary by only a few hours; predictions of the date that the freezing front reached the bottom of the ice varied by only one day (Figure 5a). This relative insensitivity to the ice thermal conductivity seems counterintuitive because k_i directly determines the heat flux through the ice. However, increasing the heat flux though the ice (by increasing k_i) increases surface temperature. Therefore, the temperature gradient effectively is decreased by increasing k_i.

Varying the density of the flooded ice from 0.75 to 0.85 g cm^{-3} led to predicted depths of flooding that ranged from 20 to 28 cm, and the predictions of the day that the freezing front reached the bottom of the ice varied by 7 d (Figure 5b). When snow densities were varied from 0.3 to 0.5 g cm^{-3}, predicted values were even more variable: the predicted depth of flooding varied by 7 cm (from 20 to 27 cm); the predicted date on which the flooded layer froze varied by 18 d (from March 7 to 25); and the predicted date that the freezing front reached the bottom of the ice varied by 26 d (from March 16 to April 11; Figure 5c). Densities of both snow and ice affected the depth of flooding because they determined the volume displacement in the hydrostatic balance formulation. These parameters also affected the rate of freezing front progression because they determine Π_x, the porosity of the snow or ice through which the freezing front was propagated. Furthermore, snow density was used to predict the thermal conductivity of the snow, which varied from 0.3 to 0.7 W m^{-1} °C^{-1} as snow densities increase from 0.3 to 0.5 g cm^{-3}. These combined effects of changing the hydrostatic balance of the ice sheet, the porosity of the snow and the snow's thermal conductivity made our model output highly sensitive to the range of snow densities that might be encountered on Antarctic sea ice [Eicken et al., 1994].

These simulations of the flood-freeze cycles at Sites A and B, along with the sensitivity analyses, demonstrate that the model is capable of simulating flood-freeze cycles and associated thermodynamic processes.

Yet, our simulation of these processes was sensitive to variations in several intrinsic ice and snow properties, which can lead to uncertainties in our predictions. Although not presented, it was also true that our simulations were sensitive to the external forcings of atmospheric temperatures, rates of snowfall, and ocean heat fluxes (discussed below). These results are discouraging because they imply that our model may be of limited use for simulating ice dynamics on large temporal and spatial scales because these parameters may be highly variable and difficult to constrain. However, our results are favorable because they imply that differences in certain factors (e.g., snow density) could have large effects on sea ice habitats, and therefore may be important in governing ecosystem responses to changes in ice dynamics. Furthermore, these results imply that the model can be used as a diagnostic tool, especially as the variables become known with greater certainty.

Microalgal Dynamics

In the previous section we showed that flood-freeze cycles can be simulated using coupled algorithms for hydrostatic balance and thermodynamics. The next step is to couple this physical model to the algal growth model for simulating microalgal dynamics.

Simulations were based on initial conditions found in the first- and second-year ice in the western Weddell Sea during the austral autumn (Table 2) and forcing variables measured at ISW-1 (Figure 3). Results from these simulations were compared to measured dynamics of microalgae in these pack ice habitats [*Fritsen et al.*, 1994; *Fritsen, 1996*; *Ackley et al.*, 1996]. The ISW-1 data set is appropriate for evaluating our predictions of dynamics in pack ice communities because it is a time-series with the supporting oceanographic and meteorologic information needed for our validation and sensitivity studies.

Surface algae. Simulations were conducted for surface ice habitats based on Sites A and B. The simulation of Site B showed net algal growth occurring in the surface flooded layer up until Julian day 72, with standing stocks reaching 9.8 mg chl$a$ m^{-2} (Figure 6). Algal growth at Site A continued 14 d longer than at Site B due to the slower progression of the freezing front through the flooded snow at Site A. Algal growth at both sites was stopped by high brine salinities and cold temperatures resulting from the freezing front passing through the surface flooded layer. Predictions of algal growth and biomass accumulations were reasonable at both sites, with the observed biomass differ-

TABLE 2. Initial conditions and coefficients used to simulate surface (Sites A and B) and bottom-ice (Sites I and J) algal dynamics at ISW-1. Values based on initial conditions found on the first day that each site was sampled. Forcing functions for atmospheric temperatures and snow fall are illustrated in Figure 3. na = not applicable.

Variable	Site A	Site B	Site I	Site J	Units
Day	56	60	77	72	------
H_i	1.1	0.85	0.43	0.5	m
h_s	0.44	0.35	0.04	0.04	m
ρ_s	0.4	0.4	0.4	0.4	g cm^{-3}
ρ_{fl}	0.8	0.8	n.a.	na	g cm^{-3}
F_w	7	7	7	7	W m^{-2}
Chl a					
surface	5	7	na	na	µg l^{-1}
bottom	na	na	67	56	µg l^{-1}

ing from the predicted values with the largest difference being only 1.5-fold (Site A, Julian day 128).

Measured nitrate concentrations (normalized to ice salinities) at both sites showed the general pattern of increasing during the initial month of the study, with slight decreases following the times when the freezing fronts were estimated to pass through the surface layers of the ice (Figures 6c and 6d; also see *Fritsen et al.*, 1994). Simulated nitrate concentrations exhibited an initial decrease during the first two days to levels that were limiting to algal growth. This was followed by a period of increasing nitrate concentrations to maximum values just prior to the time that freezing fronts passed through the surface flooded layer. Upon freezing, nutrient supply was assumed to be zero. Because the ice remained relatively warm for a brief period following freezing, the model predicted that nutrients were utilized and concentrations decreased. The general pattern of nitrate dynamics exhibited during the simulations appears to be representative of the dynamics measured at ISW-1. However, the simulated dynamics appear to underestimate the supply rate relative to its utilization. Thus, nitrate:salinity ratios are underestimated by 1.1 to 1.5-fold, which corresponds to a difference of 2 to 7 µM nitrate (at brine salinities of 34 psu).

The differences between observed and simulated nitrate dynamics may not be that surprising because nutrient flux formulations were based on empirical data of brine fluxes from the bottom of actively growing sea ice [*Arrigo et al.*, 1992]. The flux of new nutrients through sea ice to surface-flooded layers is obviously a different process than brine fluxes from the bottom of
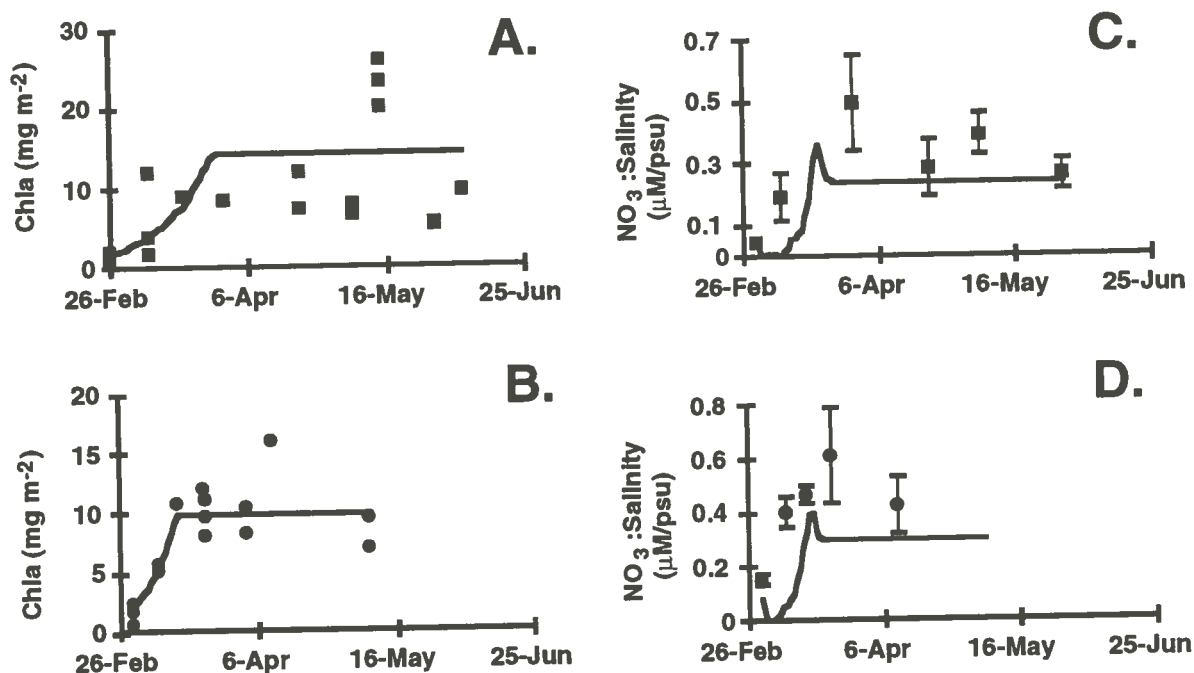
Fig. 6. Standing stocks of chlorophyll *a* and nitrate concentrations observed (symbols) and predicted (lines) in the surface of the second-year ice at ISW-1 in 1992: (a) chlorophyll at Site A; (b) chlorophyll at Site B; (c) nitrate at Site A; and (d) nitrate at Site B. Depth-integrated chlorophyll values are from the upper 40 cm at site A and from the upper 25 cm at site B (integration depths were based on the depths of flooding predicted and observed at each study site). Error bars for observed nitrate values are ±1 standard error. Nitrate concentrations are normalized to salinities to allow comparisons among sea ice cores with salinities ranging from 3 to 10 psu.

the ice. However, the simulations implied algal growth at both sites was light-limited (except for the first few days); doubling brine fluxes produced higher nitrate concentrations (which correspond better with observed values) with only a slight change in the simulated algal biomass. For instance, at Site A, a 100% increase in brine fluxes produced only a 25% increase in accumulated biomass (simulation not shown), which is within the variability of measured values. These results illustrate that the processes driving nutrient fluxes to surface habitats need to be determined, and that mechanistic (versus empirical) algorithms for nutrient fluxes may improve model performance.

Freezing front dynamics were highly sensitive to snow densities (see above). Therefore, ice-algal dynamics may be sensitive to variations in snow properties. Varying snow densities from 0.3 to 0.5 g cm^{-3} resulted in 3- to 5-fold variability in simulations of both the algal growth rates as well as the total accumulated biomass at both sites (Figure 7). As snow densities were decreased, the depth of the snow above the flooded layer increased and the depth of flooding

decreased (see above). Furthermore, both light availability and nutrient supply rates decreased. Rates of nutrient supply decreased due to the slower rate of freezing front propagation that drives seawater exchange. Light availability decreased simply because of the increase in the pathlength through which light had to pass to reach the surface ice algae. Although algal growth rates and the depth of the flooded layer were decreased in the simulations with lower snow densities, the growth period was increased. The net effect of these opposing and interactive effects was a decrease in total accumuled biomass; however, the accumulation of algal biomass as a function of snow density was highly nonlinear.

Bottom-ice algae. Simulations of ice and algal dynamics within first-year ice were initiated with initial conditions found at ISW-1 (Table 2). Atmospheric temperatures used in these simulations were those recorded at Site A (Figure 3a). No snow accumulation was noted at Site J; whereas, snow thickness at site I increased from 4 cm to 20 cm between Julian days 68 and 125 (I. Melnikov, personal communication).

Therefore, snowfall at site J was set to zero and snowfall at site I was simulated to account for the time-dependant accumulation of snow.

Simulations of ice thicknesses at both sites showed reasonable behaviors when compared to ice thickness measurements (Figure 8a). The largest discrepancies in model predictions and observed ice thicknesses occurred at site I during April when values deviated by only 4 to 5 cm.

Simulations of both sites showed rapid growth of the bottom-ice algae and accumulations of 6 to 7 mg chla m^{-2} in the bottom 2 cm of the ice (Figure 8b). The initial accumulation of algal biomass was followed by rapid decreases starting on April 14 and 15. These decreases were caused by predictions of negative ice growth (i.e., ablation at the bottom of the ice) in response to higher atmospheric temperatures (Figure 3a). The rate of decrease of bottom ice algae during ice ablation was set at 0.1 hr^{-1}; this loss rate is entirely subjective and has no basis in field observations or physical principles.

As predicted by our simulation, measured standing stocks of chla increased during the initial month of the time series (Figure 8b). Algal biomass later decreased at both study sites, but at rates slower than those used in the simulations (average = 0.18 d^{-1}). The period of

Fig. 8. Ice growth and changes in standing stock of bottom-ice algae in first-year ice forming in leads at Ice Station Weddell-1 (ISW-1): (a) ice thickness; (b) chlorophyll a concentration. Dashed line: simulations of Site J. Solid line: simulations of Site I. Triangles: observed values from Site I [after *Melnikov*, 1995]. Squares and circles: observed values from Site J.

decreasing algal biomass at Site I occurred after April 10, and coincided with an increase in atmospheric temperatures to above -15°C for several days. At Site J, the decrease in algal biomass came between April 4 and 13. Here, the period of decreasing algal biomass also coincided with increasing atmospheric temperatures, as well as a period of intense deformation activity. It is likely that the ice flooded briefly (due to ridging) and warmed during this activity. Thus, both sites experienced warming events that could have caused bottom-ice ablation; the field data are consistent with (1) the model predictions and (2) our formulations that lead to algal biomass being lost when dH_i/dt is negative.

Hoshiai [1985] also has reported decreasing algal biomass in the bottom of first-year ice in the austral autumn at near-shore study sites near Syowa Station. Grazing of the bottom-ice algae by zooplankton (e.g., krill, copepods, etc.) cannot be discounted as the mechanism for the losses observed there [*Hoshiai*, 1977], or at our sites. However, the coincidence between the model simulations (which invoke only physical processes for the losses) and the observations of ice thicknesses and algal standing stocks, would support a hypothesis that ice growth/ablation dynamics drives the
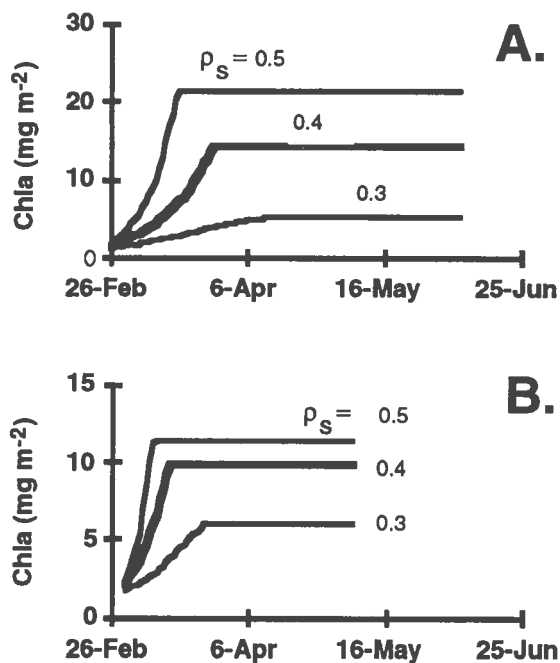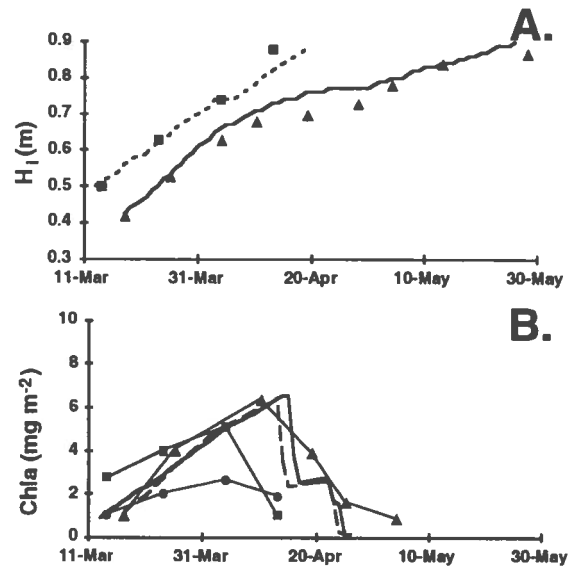
Fig. 7. Sensitivity of the simulated standing stocks of chlorophyll a in the surface of second-year ice to variations in snow densities from 0.3 to 0.5 g cm^{-3}: (a) Site A; (b) Site B.

Table 3. Coefficients and initial settings used in the simulations of ice and ice-algal dynamics in on-shelf and off-shelf settings. Forcing functions used in the simulations are illustrated in Figure 8.

Coefficient	Value	Unit
Initial Day		
on-shelf	50	---
off-shelf	90	---
Initial H_i	0.35	m
Initial h_s	0	m
ρ_s	0.4	g cm^{-3}
ρ_{fl}	0.8	g cm^{-3}
F_w		
on-shelf	2.5	W m^{-2}
off-shelf	25	W m^{-2}
N_{sw}	28	μM nitrate
N_{br}	28	μM nitrate
Initial Chl$a$		
bottom	1	μg l^{-1}
surface	1	μg l^{-1}

fluxes of particulates into the underlying water column at this time of the year.

Simulations Using Different Oceanographic Settings and Flooding Parameterizations

Ice dynamics are extremely sensitive to the flux of energy to the lower boundary of the ice. Ocean heat flux is influenced by variety of meteorologic and water column processes [e.g., *Mellor and Kantha*, 1989; *Ebert and Curry*, 1993], and thus is variable in both time and space. Potential temperature transects across the Antarctic continental shelf in the Western Weddell Sea [*Gordon,* submitted; *Huber et al.*, 1994] showed fundamental differences between shelf and off-shelf waters in this region as they relate to the oceanic heat flux. Off the shelf, the surface mixed layer lies on top of Weddell Deep Water (WDW), which has temperatures >0°C. Although these warm waters reside at depth, diffusive heat transport and entrainment processes (e.g., wind mixing, thermohaline convection, and deep-water chimney formation) generate heat fluxes into the surface mixed layer. *Martinson* [1990] estimated, through modeling studies and sensitivity analyses, that diffusive heat fluxes in the off-shelf region of the eastern Weddell Sea are large (~25 W m^{-2}) as a consequence of strong thermal gradients across rela-

tively thin pycnoclines. Surface turbulence and haline convection events create episodic entrainment of deepwater and consequently create episodic events of increased heat fluxes [*Gordon and Huber*, 1990].

The shelf region has uniform, cold temperature profiles (<−1.7°C) extending to the ocean floor. At the shelf break, deep water formation observed during one transect [*Gordon et al.*, 1993] created an effective barrier for WDW intrusion onto the shelf. Without the presence of warm WDW on the shelf, heat fluxes into surface waters are, we presume, negligible. Modeling studies of ice growth suggest that F_w values are typically low (~2 W m^{-2}) in the shelf region of McMurdo Sound [*Arrigo*, 1992; *Arrigo et al.*, 1992]. Exceptions to these general water mass distributions in relation to the shelf undoubtedly occur. However, the different oceanographic regimes undoubtedly have different oceanographic properties influencing F_w; thus F_w is likely to be highly variable within different settings of the Southern Ocean.

For our present analysis and discussion, we made simulations with variations in oceanic heat flux that represented fundamental differences between on-shelf and off-shelf settings in the Weddell Sea to illustrate (1) the general features of simulated annual to biennial cycles, (2) model sensitivities to forcing parameters, and (3) the limitations of the model.

Both simulations were forced with atmospheric temperatures, cloud cover, and rates of snow accumulation as illustrated in Figure 9, and initiated with variables and default coefficients as listed in Table 3. Oceanic heat flux and the time of initial ice formation were the only parameters varied for these simulations; ocean heat flux was 25 W m^{-2} for the off-shelf simulation [*Martinson,* 1990] and 2.5 W m^{-2} for the on-shelf simulation (as used previously for McMurdo Sound by *Arrigo et al.* [1992]). This comparison may also be representative of differences between the eastern and western Weddell Sea.

On-shelf simulations. Ice growth was quite high when F_w was set at 2.5 W m^{-2}. At the end of 1 yr, ice thickness was 185 cm (Figure 10a); therefore, the simulation was extended to project the dynamics of the system into multiple years. Extending our model predictions into summer melting seasons was not done entirely without trepidation. We recognized that our ice-growth model lacks some of the salient features that may be needed to depict melting ice floes (e.g., internal melting, flushing, and mechanical erosion). However, these processes are not quantified at present (to our
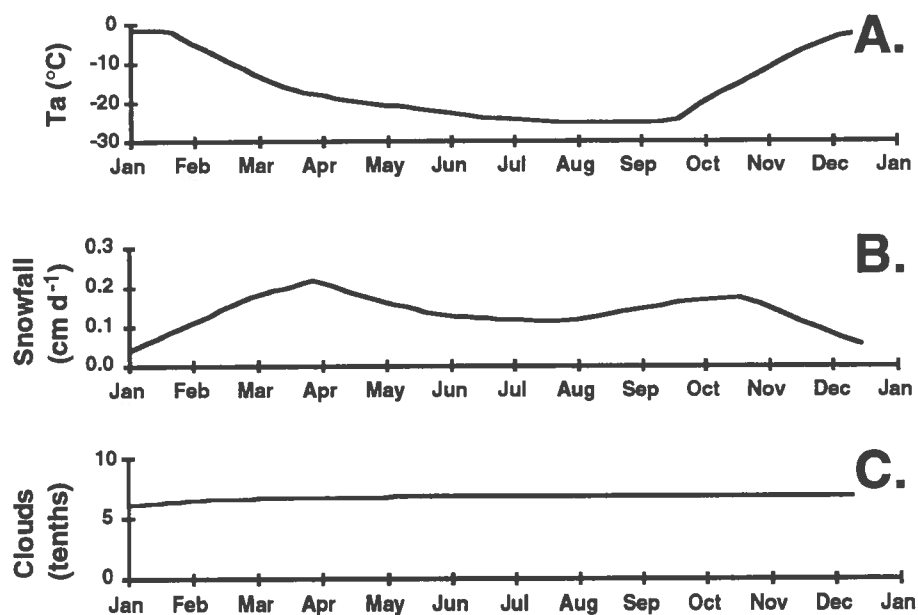
Fig. 9. Forcing variables used in simulations of annual and biennial ice and ice-algal dynamics: (a) atmospheric temperatures; (b) snow accumulation rates (based on measurements from Halley Bay [figure 9, *Eicken et al.*, 1994]); and (c) cloud coverage (in tenths). Note that we used use one-half snow fall values in our simulations (assuming that one-half of the snow would either fall directly into leads or be trapped in leads during snow reworking events).

knowledge) and could be parameterized in future work. Overall, the results from this simulation showed some patterns consistent with previous observations, as well as those inconsistent with our current understanding of ice algal distributions.

This simulation showed ice-flooding in January which decreased the amount of snow above sea level to only 13 cm. Freezing fronts passed through the flooded layer and reached the bottom of the ice in early April, leaving 27 cm of snow on top of 215 cm of consolidated ice. The consolidated ice at this time was comprised of 185 cm of sea ice and 30 cm of ice formed from freezing the flooded snow. Snow accumulation occured again in the second winter to a maximum depth of 65 cm in late January when flooding occured to a depth of 47 cm (Figure 10b). Freezing fronts again propagated through the flooded layer and reached the bottom of the ice by the last week in May. It is important to note that the timing of the flood-freeze cycles roughly corresponded to the timing of the flooding and freezing observed at ISW-1, despite the fact that this simulation was initiated almost 1 yr earlier and was forced with general forcing functions that were not specific for the ISW-1 studies. These results imply that simulations may be robust when predicting general ice dynamics. Furthermore, they imply that flood-freeze cycles may be common given the general forcings of the Southern Ocean.

Algal dynamics during these simulations showed a bloom of bottom-ice algae during the first autumn when the new ice was actively thickening (Figure 10c). Biomass reached 9.5 mg chl$a$ m^{-2} by mid-May and persisted through the austral winter seasons. Ice thickness decreased in late November due to atmospheric warming, and bottom-ice ablation was predicted; at this time, the simulated bottom-ice community was released into the water column.

Surface communities were predicted to begin growing when the ice warmed in late November with biomass reaching a maximum of 3.1 mg chl$a$ m^{-2} as nutrients in the brine became depleted. Additional algal biomass grew and accumulated when the ice flooded in January (i.e., introduction of new nutrients to the ice surface was predicted). Algal growth once again became nutrient limited when biomass reached 5.0 mg chl$a$ m^{-2} on January 15. Freezing fronts began propagating through the flooded layer on January 30, which resupplied the surface habitat with new nutrients. During this growth phase, biomass accumulated until March 6 (to 19 mg chl$a$ m^{-2}) before the surface layer froze completely and algal growth stopped due to low
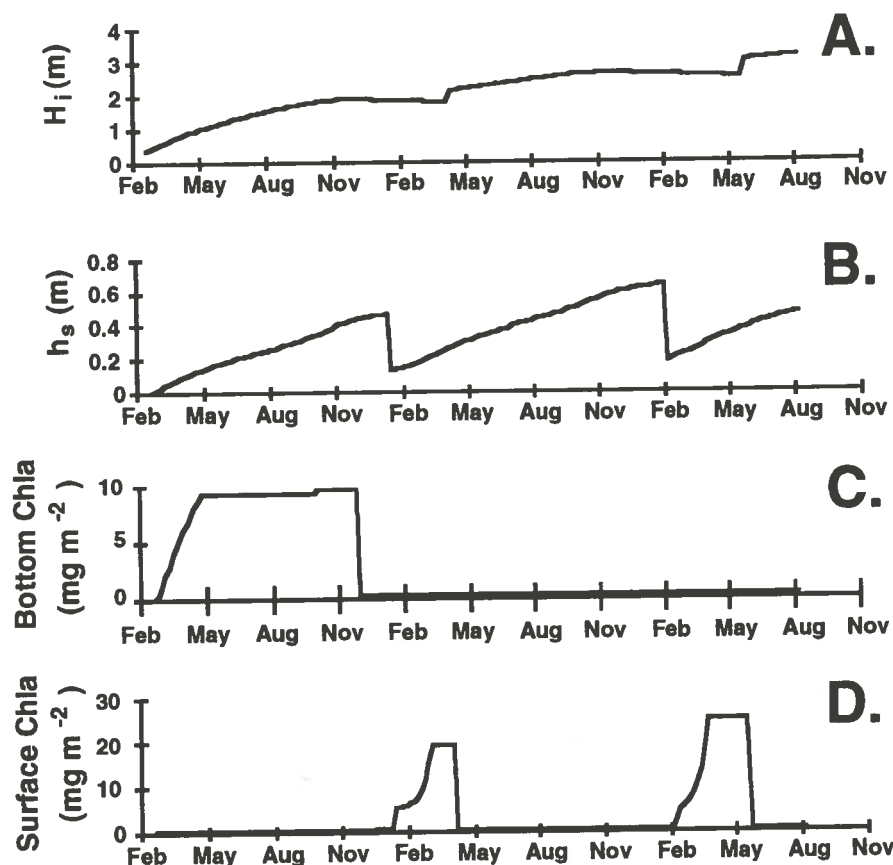
Fig. 10. Model predictions with F_W set at 2.5 W m^{-2} to simulate ice dynamics in an on-shelf oceanographic setting: (a) ice thickness, (b) snow thickness, (c) chlorophyll a in bottom-ice, and (d) chlorophyll a in surface ice.

temperatures and high salinities. The decrease in surface standing crop depicted in Figure 10d is due to the incorporation of the algal biomass into the ice interior upon the completion of the flood-freeze cycle. As mentioned previously, we have not attempted to model the newly created interior communities.

No accumulation of algal biomass was predicted at the bottom of the ice during the rest of the simulation due to the combined effects of low light and bottom-ice ablation during the subsequent austral springs. In contrast, growth of algae at the ice surface was predicted for the first week of February and 25 mg chl$a$ m^{-2} accumulated by March 25 (when freezing fronts had propagated through the flooded layer). The subsequent decrease in standing stock during May (Figure 10d) is due to the internalization of this algal bloom.

Off-shelf simulations. The ocean heat flux was increased to 25 W m^{-2} to simulate an off-shelf setting, and the model was initiated on April 1 because most ice growth in off-shelf regions starts later than in on-shelf

regions [*Zwally et al.*, 1983]. These conditions resulted in a maximum ice thickness of 86 cm during September (Figure 11a) compared to a maximum of 190 cm during December in the on-shelf simulation. Snow thickness reached a maximum of 34 cm on November 17 before surface flooding reduced the thickness of the snow above sea level to 12 cm (Figure 11b).

Bottom-ice algae were predicted to accumulate to 2.4 mg chl$a$ m^{-2} by May 11 (Figure 11c). At this time, ice thickness was still < 70 cm and snow thickness was < 10 cm. This compares to 9.5 mg chl$a$ m^{-2} predicted for the autumnal accumulation in the bottom-ice habitat during the on-shelf simulation, despite thicker ice and snow. The primary difference between the two simulations was that the off-shelf simulation was initiated later in the season; therefore, less total light was available for growth of bottom-ice algae before winter darkness. This result demonstrates a sensitivity of the system to initial conditions (in this case, the date for initiation of ice formation).
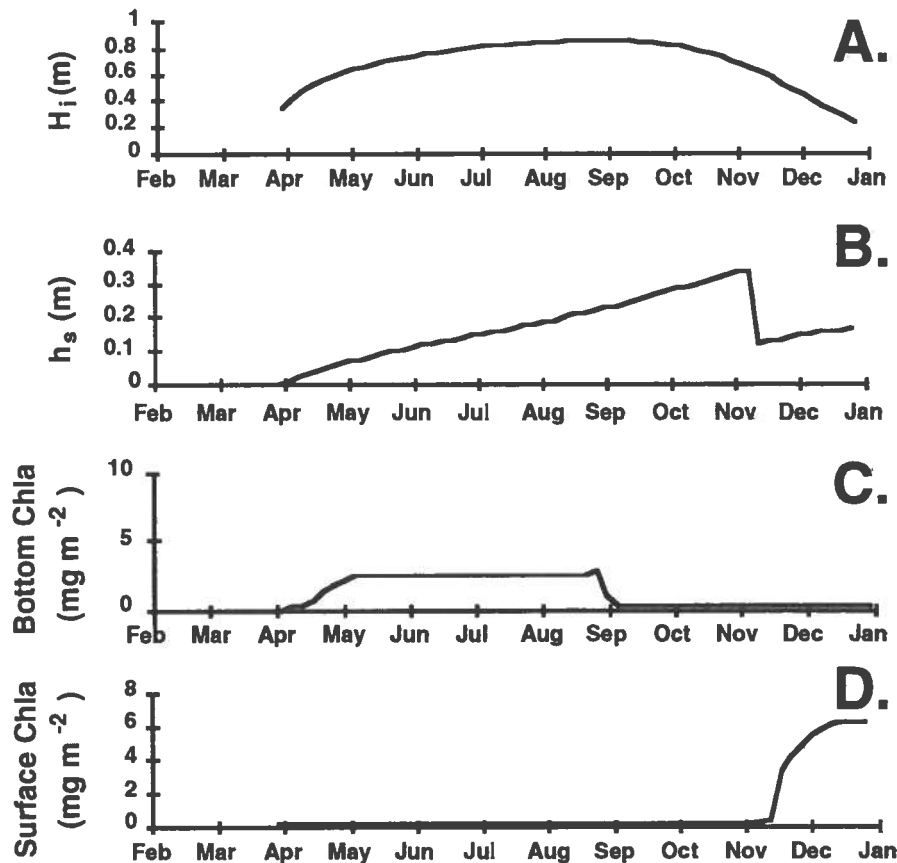
Fig. 11. Model predictions with F_W set at 25 W m^{-2} to simulate ice dynamics in an off-shelf oceanographic setting: (a) ice thickness, (b) snow thickness, (c) chlorophyll a in bottom-ice, and (d) chlorophyll a in surface ice.

Simulated algal growth in the surface habitat started in early November when the ice was warming, yet had not warmed enough to be permeable to flooding. Soon thereafter (November 17), the ice flooded and algal biomass grew to 6.3 mg chl$a$ m^{-2} (Figure 11c) before the flooded layer froze. At this time, the total ice thickness (sea ice thickness plus the frozen flooded layer) was 45 cm with 17 cm of snow. The freezing front had not reached the bottom of the sea ice, and the ice was ablating rapidly. The dynamics of decaying sea ice, especially where ice thicknesses are small, are not well known. Therefore, when the sea-ice thickness reached 20 cm the simulation was terminated.

In both the on-shelf and off-shelf simulations, the biomass in the bottom-ice habitats persisted through the winter. These results contrast with the seasonal dynamics of bottom-ice algal communities observed at ISW-1 [*Fritsen et al.*, 1994; *Ackley et al.*, 1996] and in the pack ice near Swoya station [*Hoshiai*, 1985]. Losses are currently parameterized only to occur when net ice growth is negative (i.e., during bottom-ice ablation), and the losses at ISW-1 may be attributable to a short atmospheric warming event that led to bottom-ice ablation (see above). Because we used monthly averages for the on-shelf and off-shelf simulations, net ice loss was not predicted until spring. Furthermore, ocean heat fluxes were held constant. This is probably not the case in the real world. Therefore, fluctuating atmospheric temperatures and oceanic heat fluxes may be responsible for losses observed during field studies that were accounted for in these longer-term simulations. The apparent discrepancy between the model predictions and observations from field studies further illustrates that losses through either biological processes (such as grazing, respiration, viral mortality, etc.) or physical processes (e.g., ablation or brine dilution) need to be examined in more detail in order to discern the how algal biomass is transferred within and from the sea ice.

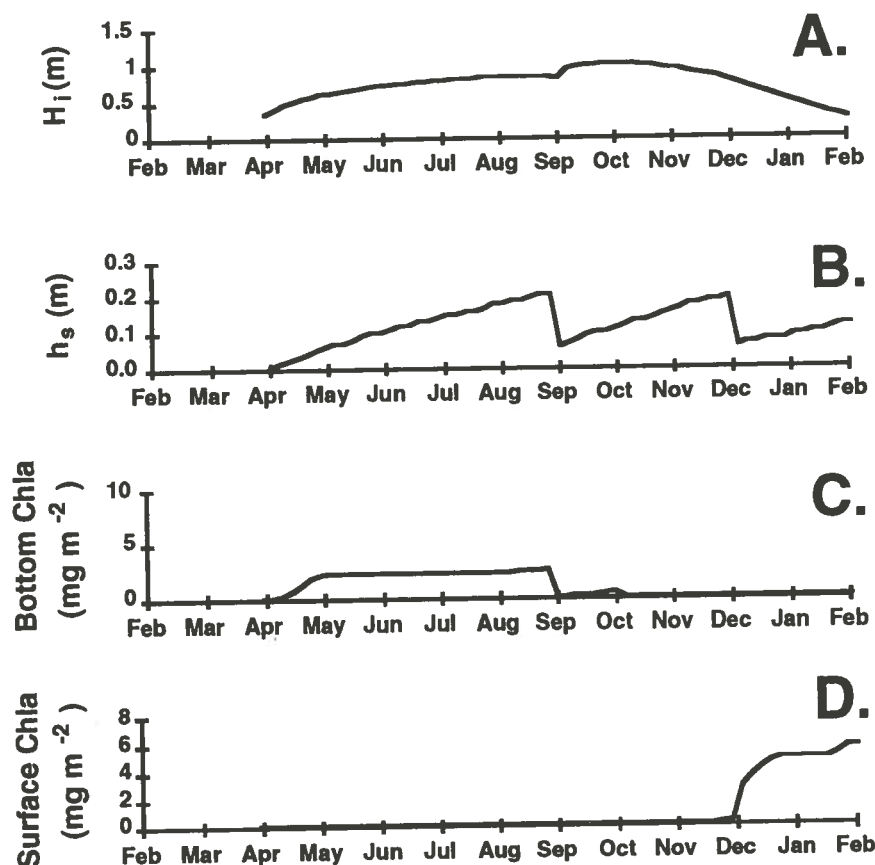Surface flooding occurred during both on-shelf and

Fig. 12. Model predictions with surface flooding allowed at any time that the predicted freeboard height became negative: (a) ice thickness, (b) snow thickness, (c) chlorophyll *a* in bottom-ice, and (d) chlorophyll *a* in surface ice.

off-shelf simulations in the austral spring (Figures 10b and 12b). Flooding was precluded during the winter despite snow thicknesses that depressed the ice surface below sea level in our off-shelf simulation (e.g., for ρ_s = 0.25 g cm^{-3}, a snow thickness more than one-fourth the ice thickness will depress the ice below sea level; Equation 5 and *Ackley et al.* [1990]). Negative free-board heights have been observed both without surface flooding (S. Ackley, personal observation), and with snow-induced flooding (including winter observations by *Fritsen* [1996]). Brief periods of atmospheric warming during the winter (which were not prescribed during these simulations) could allow the ice to become permeable and allow surface flooding to occur during winter. Also, cracks could act as conduits for snow-induced flooding. Knowledge about the exact mechanisms that control snow-induced surface flooding remains equivocal.

Flooding parameterization. A simulation was run with ocean heat flux at 25 W m^{-2} (i.e., simulating an off-shelf setting) and the ice permeable to flooding at all times of the year. The dynamics of both the ice and the ice algae were changed markedly. Ice thickness reached a maximum of 103 cm on October 8 (Figure 12a); this was 20% thicker and an additional month of ice growth compared to simulations in which flooding was not allowed until the ice was permeable. Most of the added ice thickness was due to 15 cm of the insulating snow cover that was incorporated into the ice matrix during the flood-freeze cycle around August 29 (Figure 12b).

We predicted that when the ice flooded in August, the surface flooded layer froze within 5 d. Therefore time and light availability was not sufficient for algal growth to produce appreciable biomass within the surface habitat at this time (Figure 12d). When the ice flooded again on December 7, algal growth occurred to an accumulation of 4.9 mg chl*a* m^{-2}. The algae became limited by nutrients during January. The freezing front began propagating again when air temperatures de

creased in the austral autumn. Reductions in nutrient limitation allowed for additional accumulation of algal biomass (up to 5.6 mg chl$a$ m^{-2}) until the surface layer became frozen; then the biomass was incorporated into the consolidated ice matrix. Thus, algal biomass produced in the surface habitats was comparable between the simulations, with and without constraints on flooding (5.6 and 6.3 mg chl$a$ m^{-2}, respectively), despite the changes in the timing and extent of surface flooding.

Bottom-ice algae also grew in the austral autumn in our simulations. They grew from the first week in August until the first flood-freeze cycle released them into the water column (due to our assumption that the ice is isothermal below a propagating freezing front, which leads to bottom-ice ablation when ocean heat fluxes are greater than zero). Upon completion of the flood-freeze cycle on September 3, bottom-ice algae grew and accumulated additional biomass for a brief period (until October 8; Figure 12c) until the ice was predicted to thin in response to warming atmospheric temperatures.

The net effect of simulating ice flooding anytime freeboard heights became negative was to (1) increase maximum ice thickness, (2) decrease accumulation of snow cover, (3) simulate additional growth periods for bottom-ice algae, (4) delay the timing of algal growth in the surface habitat from November to December, and (5) decrease the accumulation of biomass in the surface habitat by a nominal 10%. Because the factors controlling permeability of sea ice to flooding appear to have profound effects on both the ice geophysics and the ice microbiota, it seems reasonable that this process should be studied in greater detail in the future.

CONCLUSION

When viewed as a diagnostic tool, the model showed basic features that may govern sea-ice and ice-algal dynamics. These features imply that the ratio of the conductive heat flux through the ice (controlled by atmospheric temperatures, snowfall and intrinsic snow and ice properties) and the rate of snow accumulation relative to the oceanic heat flux controls ice growth and flood-freeze cycles which, in turn, control the timing, location and magnitude of algal growth within both the surface and bottom ice habitats. Thus, the magnitude of primary production in the ice habitats as well as the physical structuring of the sea-ice ecosystem is likely to be altered by variations in local weather patterns and/or climate variability. The consequences of these varia-

tions are unknown; yet, they are likely to be propagated throughout the Southern Ocean ecosystem.

REFERENCES

Ackley, S. F., C. H. Fritsen, V. I. Lytle, and C. W. Sullivan, Freezing driven upwelling in Antarctic sea ice biological systems, *Proc. NIPR Symp. Polar Biol., 9,* 45-59, 1996.

Ackley, S. F., M. Lange, and P. Wadhams, Snow cover effects on Antarctic sea ice thickness, *in Sea Ice Properties and Processes*, edited by S.F. Ackley and W.F. Weeks, *CRREL Monogr., 90-1,* 300, 1990.

Ackley, S. F., and C. W. Sullivan, Physical controls on the development and characteristics of Antarctic sea ice biological communities – a review and synthesis, *Deep-Sea Res., 41,* 1583-1604, 1994.

Allison, I., The East Antarctic sea ice zone: Ice characteristics and drift, *Geojournal, 18,* 103-115, 1989.

Arrigo, K. R., *A Simulated Antarctic Fast-Ice Ecosystem*, Ph.D. Dissertation, University of Southern California, Los Angeles, 1992.

Arrigo, K. R., G. Dieckmann, M. Gosselin, D.H. Robinson, C.H. Fritsen, and C. W. Sullivan, A high resolution study of the platelet ice ecosystem in McMurdo Sound, Antarctica: Biomass, nutrient, and production profiles within a dense microalgal bloom, *Mar. Ecol. Prog. Ser., 127,* 255-268, 1995.

Arrigo, K. R., and C. W. Sullivan, The influence of salinity and temperature covariation on the photophysiological characteristics of Antarctic sea ice microalgae, *J. Phycol., 28,* 746-756, 1992.

Arrigo, K.R., C. W. Sullivan, A high resolution bio-optical model of microalgal growth: Tests using sea-ice algal community time-series data, *Limnol. Oceanogr., 39,* 609-631, 1994.

Arrigo, K. R., C. W. Sullivan, and J. N. Kremer, A bio-optical model of Antarctica sea ice, *J. Geophys. Res., 96(C6),* 10,581-10,592, 1992.

Arrigo, K.R., C. W. Sullivan, and J. N. Kremer, A simulated Antarctic fast-ice ecosystem, *J. Geophys. Res., 98(C4),* 6929-6946, 1993.

Assur, A., Composition of sea ice and its tensile strength, in *Arctic Sea Ice, National Research Council.,* Pub. *59,* pp. 106-138, U.S. National Academy of Sciences, 1958.

Brine, D. T., and M. Iqbal, Diffuse and global solar spectral

irradiance under cloudless skies, *Solar Energy*, *30*, 447-453, 1983.

Bunt, J. S., Diatoms of Antarctic sea-ice as agents of primary production, *Nature*, *199*, 1255-1257, 1963.

Cox, G. F. N., and W. F. Weeks, Equations for determining the gas and brine volumes in sea-ice samples, *J. Glaciol.* *29*, 306-316, 1983.

Cox, G. F. N., and W. F. Weeks, *Profile Properties of Undeformed First-Year Sea Ice, CRREL Monogr.*, *57*, 1988.

Daly, K., Overwintering development, growth, and feeding of larval *Euphausia superba* in the Antarctic marginal ice zone, *Limnol. Oceanogr.*, *35*, 1564-1576, 1990.

Dugdale, R. C., and J. J. Goering, Uptake of new and regenerated forms of nitrogen in primary productivity, *Limnol. Oceanog.*, *12*, 196-206, 1967.

Ebert, E. E., and J. A. Curry, An intermediate one-dimensional thermodynamic sea ice model for investigating ice-atmosphere interactions, *J. Geophys. Res.*, *98(C6)*, 10,085-10,109, 1993.

Eicken, H., Salinity profiles of antarctic sea ice: Field data and model results, *J. Geophys. Res.*, *94(C6)*, 8193-8206, 1992.

Eicken, H., M. A. Lange, H. W. Hubberten, and P. Wadhams, Characteristics and distribution patterns of snow and meteoric ice in the Weddell Sea and their contribution to the mass balance of sea ice, *Ann. Geophys.*, *12*, 80-93, 1994.

El-Sayed, S. Z., Productivity in the Antarctic waters – a reappraisal, in *Marine Phytoplankton and Productivity*, edited by O. Holm Hansen, L. Bolis, and R. Gilles, pp. 19-34, Springer-Verlag, Berlin, 1984.

Eppley, R. W., Temperature and phytoplankton growth in the sea, *Fishery Bulletin*, *70*, 1063-1085, 1972.

Franeker, J. A., Top predators as indicators for ecosystem events in the confluence zone and marginal ice zone of the Weddell and Scotia Seas, Antarctica, November 1988 to January 1989 (EPOS, Leg 2), *Polar Biol.*, *12*, 93-102, 1992.

Fritsen, C. H., *Ecology of Antarctic Pack-Ice Microbial Communities*, Ph.D. Dissertation, University of Southern California, Los Angeles, 1996.

Fritsen, C. H., R. Itturiaga, and C. W. Sullivan, Influence of particulate matter on spectral irradiance fields and energy transfer in the eastern Arctic Ocean, *SPIE, 1750 (Ocean Optics XI)*, 527-541, 1992.

Fritsen, C. H., V. I. Lytle, S. F. Ackley and C. W. Sullivan, Autumn bloom of Antarctic pack-ice algae, *Science, 266*, 782-784, 1994.

Fritsen, C. H., and C. W. Sullivan, Microbial distributions and dynamics in the western Weddell Sea, in *Antarctic Communities Part II: Community structure and function*, edited by B. Battaglia, J. Valencia, and D. Walton, (in press).

Garrison, D. L., S. F. Ackley, and C. W. Sullivan, Sea ice microbial communities in Antarctica, *Bioscience, 36*, 243-250, 1986.

Garrison D. L., and K. R. Buck, Surface-layer sea ice assemblage in Antarctic pack ice during the austral spring: envi-

ronmental conditions, primary production, and community structure, *Mar. Ecol. Prog. Ser.*, *75*, 161-172, 1991.

Gordon, A. L., and B. A. Huber, Southern ocean winte mixed layer, *J. Geophys. Res.*, *96(C7)*, 11,655-11,672 1990.

Gordon, A. L., Western Weddell Sea thermohaline stratifica tion, in *Oceanology of Antarctic Continental Margin* edited by S. Jacobs, *Antarct. Res. Ser.* (submitted).

Gordon, A. L., and V. Lukin, Weddell Sea exploration fro ice station, *Eos, 74*, 121-126, 1993.

Grenfell, T. C., A radiative transfer model for sea ice wi vertical structure variations, *J. Geophys. Res.*, *96(C9* 16,991-17,001, 1991.

Grenfell, T. C., and D. K. Perovich, Radiation absorptic coefficients of polycrystelline ice from 400 nm to 14(nm, *J. Geophys. Res.*, *86*, 7447-7450, 1981.

Grossi, S. M., and C. W. Sullivan, Sea ice microb communities. V. The vertical zonation of diatoms in Antarctic fast ice community, *J. Phycol.*, *21*, 401-40 1985.

Grossi, S. M., S. T. Kottmeier, R. L. Moe, G. T. Taylor, a C. W. Sullivan, Sea ice microbial communities. VI. Grow and primary production in bottom ice under graded sn cover, *Mar. Ecol. Prog. Ser.*, *35*, 153-164, 1987.

Horner, R., S. F. Ackley, G. S. Dieckmann, B. Gulliksen, Hoshiai, L. Legendre, I. A. Melnikov, W. S. Reeburgh, Spindler, and C. W. Sullivan, Ecology of sea ice biota Habitat, terminology, and methodology, *Polar Biol.*, 417-427, 1992.

Hoshiai, T., Seasonal changes of ice communities in the ice near Swoya Station, Antarctica, in *Polar Oceans*, edi by M.J. Dunbar, pp., 307-317, Arctic Institute of No America, Calgary, 1977.

Hoshiai, T., Autumnal proliferation of ice-algae in Antar sea-ice, in *Antarctic Nutrient Cycles and Food We* edited by W.R. Seigfried, P.R. Condy, and R.M. Laws, 89-92, Springer-Verlag, Berlin, 1985.

Huber, B. A., P. A. Mele. W. E. Haines. A. L. Gordon. an I. Lukin, Ice Station Weddell – 1: CTD/hydrographic d *Technical Report LDEO-94-2 of Lamont-Doherty E Observatory*, Columbia University, Palisades NY, 1994.

Kirk, J. T. O., *Light and Photosynthesis in Aquatic Eco tems*, pp. 24-41, Cambridge University Press, Cambri England, 1983.

Kottmeier, S. T., and C. W. Sullivan, Bacterial biomass production in pack ice of Antarctic marginal ice e zones, *Deep-Sea Res.*, *37*, 1311-1330, 1990.

Kremer, J. N., and S. W. Nixon, *A Coastal Marine Eco tem: Simulation and Analysis*, Springer-Verlag, New Y 1978.

Lepparanta, M., A review of analytical models of sea growth, *Atmosphere-Ocean.*, *31*, 123-138, 1993.

Lytle, V. I., and S. F. Ackley, Heat Flux through sea id the western Weddell Sea: Convective and conductive tr fer processes, *J. Geophys. Res.*, *101(C4)*, 8853-8868, 1'

Martinson, D. G., Evolution of the southern ocean w mixed layer and sea ice: open ocean deepwater form

and ventilation, *J. Geophys. Res.*, *95(C7)*, 11,641-11,654, 1990.

Maykut, G. A., The surface heat and mass balance, in *The Geophysics of Sea Ice*, edited by N. Untersteiner, pp., 395-464, Plenum Press, NY, 1986.

Maykut, G. A., and D. K. Perovich, The role of shortwave radiation in the summer decay of a sea ice cover, *J. Geophys. Res.*, *92(C7)*, 7032-7044, 1987.

Maykut, G. A., and N. Untersteiner, Some results from a time-dependent thermodynamic model of sea ice, *J. Geophys. Res.*, *76*, 1550-1575, 1971.

McPhee, M. G., and D. G. Martinson, Turbulent mixing under drifting pack ice in the Weddell Sea, *Science*, *263*, 218-221, 1994.

Mellor, G. L., and L. Kantha, An ice-ocean coupled model, *J. Geophys. Res.*, *94*, 10937-10954, 1989.

Melnikov, I., An in situ experimental study of young sea ice formation on an Antarctic lead, *J. Geophysic. Res.*, *100 (C3)*, 4673-4680, 1995.

Mobley, C., *Light and Water: Radiative Transfer in Natural Waters*, pp., 265-284, Academic Press, San Diego, 1994.

Morel, A., Available, usable, and stored radient energy in relation to marine photosynthesis, *Deep-Sea Res.*, *25*, 673-688, 1978.

Perovich, D. K., Theoretical estimates of light reflection and transmission by spatially complex and temporally varying sea ice covers, *J. Geophys. Res.*, *95(C6)*, 9557-9567, 1990.

Reeburgh, W. S., Fluxes associated with brine motion in growing sea ice, *Polar Biol.*, *3*, 29-33, 1984.

Schlatter, T. W., The local surface energy balance and sub-surface temperature regime in Antarctica, *J. Appl. Meteorol.*, *11*, 1048-1062, 1972.

Stavn, R. H., and A. D. Weidemann, Shape factors, two-flow models, and the problem of irradiance inversion in estimating optical parameters, *Limnol. Oceanogr.*, *34*, 1426-1441, 1989.

Stefan, J., Uber die Theorie der Eisbildung, insbesondere uber Eisbildung im Polarmeere, *Ann. Phys., 3rd Ser.*, *42*, 269-286, 1891.

Sullivan, C. W., A. C. Palmisano, S. Kottmeier, S. M. Grossi, and R. Moe, The influence of light on growth and development of the sea-ice microbial community of McMurdo Sound, in *Antarctic Nutrient Cycles and Food Webs*, edited by W.R. Seigfried, P.R. Condy, and R.M. Laws, pp. 78-83, Springer-Verlag, Berlin, 1985.

Sverdrup, H. U., M. W. Johnson, and R. H. Fleming, *The Oceans*, Prentice Hall, Englewood Cliffs, N.J., 1947.

Wakatsuchi, M., and N. Ono, Measurements of salinity and volume of brine excluded from growing sea ice, *J. Geophys. Res.*, *88(C5)*, 2943-2951, 1983.

Zwally, H. J., W. J. Campbell, F. D. Carsey, and P. Gloersen, *Antarctic Sea Ice, 1973-1976: Satellite Passive Microwave Observations*, *NASA Spec. Publ.* 45, Washington D.C., 1983.

Stephen F. Ackley, Cold Regions Research and Engineering Laboratory, Army Corp of Engineers, Hanover, NH, 03755.

Christian H. Fritsen, Department of Biology, Montana State University, Bozeman, MT 59717

James N. Kremer, Department of Marine Sciences, Avery Point Campus, University of Connecticut, Groton, CT 06340.

Cornelius W. Sullivan, Department of Biological Sciences, University of Southern California, Los Angeles, CA 90089.

PRIMARY PRODUCTIVITY OF NEAR SURFACE COMMUNITIES WITHIN ANTARCTIC PACK ICE

Kevin Arrigo[1], Denise L. Worthen[2], Paul Dixon[3], and Michael P. Lizotte[4]

A numerical model of the Antarctic pack ice ecosystem has been developed for the purpose of investigating the spatial and temporal patterns of primary production. The sea ice habitat was described using a simplification of an existing one-dimensional fast-ice ecosystem model. Model results show that of the 35.7 Tg C produced annually in the Antarctic ice pack, 75% was associated with first-year ice and nearly 50% occurred in the Weddell Sea. Although the productivity per unit ice surface was greatest in January, total production peaked in November due to the more extensive sea ice cover. Rates of production in the Weddell Sea were more than twice as high as in the Ross Sea, despite reduced light from a thicker snow cover, because of more extensive surface flooding which provides additional nutrients to surface communities. Model results demonstrate that the thickness of the snow cover in combination with the proportion of first-year ice in a given region are fundamental in controlling primary production within sea ice over large scales.

1. INTRODUCTION

The advance and retreat of annually forming sea ice around Antarctica is among the most dynamic features of the global ocean. When present, pack ice increases the albedo of the ocean, alters the optical properties of the water column, and restricts heat and gas exchange with the atmosphere. Pack ice also acts as a habitat for rich microbial communities [*Garrison et al.*, 1986; *Smetacek et al.*, 1992] and, with an areal coverage ranging from 4-20×10^6 km² [*Zwally et al.*, 1979], is one of the largest ecosystems on earth.

Algal communities are known to flourish within the distinct micro-habitats which are created when pack ice forms and ages [*Garrison et al.*, 1986; *Smetacek et al.*, 1992; *Ackley and Sullivan*, 1994]. In the early stages of pack ice formation, dense concentrations of frazil ice develop rapidly under turbulent conditions [*Ackley and Sullivan*, 1994]. When the sea surface calms, ice crystals float to the sea surface, often scavenging particles such as microalgae as they rise. The floating ice crystals then coalesce into semi-consolidated grease ice and eventually, into pancake ice [*Garrison et al.*, 1983, 1990]. Additional freezing fuses ice pancakes together to form a continuous ice sheet. Subsequent vertical ice growth then proceeds as columnar ice crystals extend from the lower frazil ice surface into the water column. In land-fast ice, the lower margin of the columnar ice (the skeletal layer) is frequently inhabited by an abundance of ice microalgae. These bottom ice communities are generally absent or much less prevalent within pack ice [*Legendre et al.*, 1992]. As the pack ice ages, an additional layer forms at the freeboard (sea) level in response to increasing air temperatures during the spring and summer. The freeboard layer is characterized by a cavity within the ice surrounded above and below by relatively porous (high brine volume) sea ice.

Sea ice microalgae growing within these micro-habitats of pack and land fast ice are subject to limitation by the available light and nutrients. In land fast ice, the growth of sea ice microalgae in the skeletal layer is determined primarily by salinity [*Arrigo and Sullivan*, 1992] and by the thickness of the overlaying snow cover through its effect on vertical light attenuation [*Arrigo et al.*, 1991]. In contrast, pack ice algae frequently grow at or near the sea ice surface where light levels are gener-

[1]NASA Goddard Space Flight Center, Oceans and Science Branch, Code 971.0, Greenbelt, Maryland
[2]Science Systems Applications, Inc., Lanham, Maryland
[3]Scripps Institution of Oceanography, University of California, San Diego, La Jolla, California
[4]Department of Biology and Microbiology, University of Wisconsin, Oshkosh, Oshkosh, Wisconsin
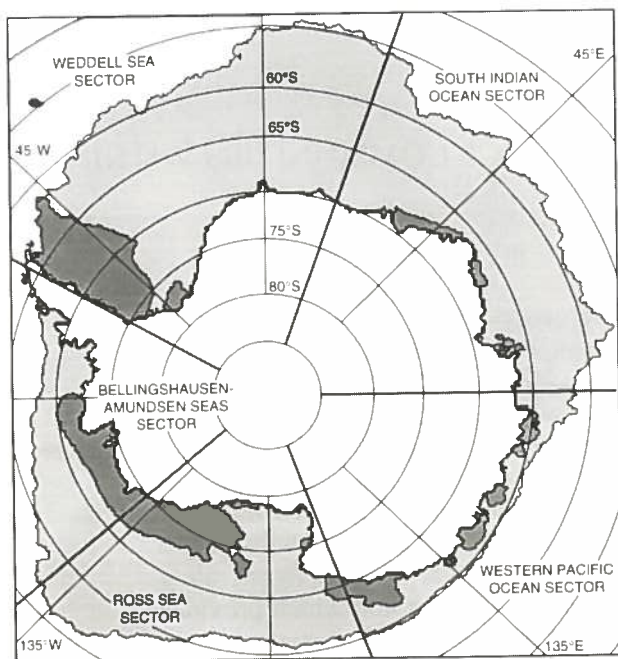
Fig. 1. Map of the Southern Ocean showing the minimum (dark gray) and maximum (light gray) sea ice extent during the simulation (1989-90) as well as the boundaries of the five geographic sectors referred to in the text.

ally high. Under these conditions, pack ice microalgae have been found to have high photosynthetic capacities, comparable to phytoplankton from the same region [*Lizotte and Sullivan*, 1992]. These pack ice photosynthetic capacities are approximately an order of magnitude greater than values reported for land-fast algae [e.g., *Palmisano et al.*, 1987; *Arrigo et al.*, 1993b].

Although the surface and near surface communities often have adequate light levels for growth, the availability of nutrients for these communities is often restricted (for details on nitrogen metabolism of fast-ice microalgae, see *Priscu and Sullivan*, this volume). Measurements of salinity in the cavity of the freeboard layer indicate that this layer is infiltrated by seawater which provides the nutrients required by the algal community [*Ackley and Sullivan*, 1994]. However, this supply of nutrients depends on the porosity of the surrounding ice. For the algal communities growing at the snow/ice interface, surface flooding, caused by snow loading and submersion of the ice pack, is an important source of nutrients. Such surface flooding occurs over 15-30% of the ice pack in Antarctica [*Wadhams et al.*, 1987]. Although snow cover has the negative effect of reducing the amount of light available for algal growth, it is also responsible for providing nutrients to the surface community. Surface communities (infiltration and free-

board) are responsible for the majority of sea ice productivity in Antarctic sea ice [*Legendre et al.*, 1992].

While our understanding of sea ice microalgal physiology and the sea ice ecosystem continues to increase, little is presently known about either the large-scale horizontal distribution of pack ice algae or their contribution to total regional productivity due to the difficulty inherent in sampling ice covered regions. The goal of the present study was to utilize our present knowledge of pack ice geophysics and microalgal physiology to model the temporal and large-scale horizontal variation in standing crop and rates of primary production of ice algae in the Southern Ocean. Because ice algal growth is highly sensitive to snow thickness, this study was dependent upon the availability of snow cover data at the appropriate temporal and spatial scales. In particular, we wished to derive an estimate of primary production within the ice sheet to determine how much fixed carbon might be exported to other trophic levels. This information will lead to an increased understanding of Southern Ocean ecosystems as well as improve carbon budgets for this region.

2. THE MODEL

2.1 Description

The numerical model used in the present study calculates the spatial and temporal variability of primary productivity in Antarctic sea ice (Figure 1) between October 1, 1989 and April 30, 1990 using a modified version of a one-dimensional productivity model described in *Arrigo et al.* [1993a] and *Arrigo and Sullivan* [1994]. The model includes components describing 1) atmospheric spectral radiation (400-700 nm) as a function of time, date, latitude, and cloud cover, 2) in-ice bio-optics, 3) sea ice geophysics, and 4) biological dynamics.

The model domain is based on the Special Sensor Microwave/Imager (SSM/I) grid. Using daily maps of sea ice concentration on this grid, productivity and biomass were calculated for any pixel with an ice concentration exceeding 0.50 (50%). The physical structure of the pack-ice ecosystem was simplified for modeling purposes (Figure 2). Productivity was allowed in either an infiltration (0.02 m thick) layer at the ice/snow interface or within an internal freeboard (0.10 m thick) layer. A uniform (0.10 m thick) ice layer separated the infiltration and freeboard layers. The thickness of each of these layers was held constant for the length of the integration. Simulations made using early versions of the model showed that holding the layer thickness constant had

little effect on model results. Algal growth within interior (other than freeboard) layers and the bottom ice layer was neglected because these communities represent only a small fraction of pack ice production [*Legendre et al.*, 1992]. The model was run with one hour time steps at a vertical resolution of 0.5 cm in the infiltration layer, 1 cm in the freeboard layer, and a horizontal resolution of 625 km^2.

The thickness of ice below the freeboard layer was varied spatially in order to represent both relatively thin first-year ice and relatively thick multi-year ice in the model. The initial spatial distribution and thickness of multi-year ice were derived from the SSM/I sea ice distribution at the day of minimum ice extent in February 1989. On this date, ice with concentration greater than or equal to 0.8 was specified to have a bottom ice thickness of 1.28 meters and ice with concentration less than or equal to 0.1 was specified to have a bottom ice thickness of 0.53 meters. Linear interpolation was used to smoothly vary the ice thickness between these two ice concentrations. Ice which was present on the first day of the model integration which had not been specified with a multi-year ice thickness was initialized with a bottom ice thickness of 0.53 meters. Thus, for the purposes of this model, first-year ice was defined as ice with a total thickness of 0.75 meters, and multi-year ice was defined as ice with a total thickness greater than 0.75 meters.

Both multi-year and first-year ice were initialized on

Fig. 3. Relative frequency distributions of observed and modeled snow thickness in the Weddell Sea for all times and locations for which data were available. The dashed line refers to the estimates made using the SSM/I data as described in *Arrigo et al.* [1996]. The solid line refers to the estimates made after subdividing each pixel into the nine grid points as described in the text. The snow depth for each grid point was included in the frequency distribution. Over 1400 in situ measurements of snow thickness were made in the Weddell Sea during 1986, 1989, and 1992.

October 1 with a uniform Chl *a* concentration of 1 mg m^{-3}, consistent with ice-core observations. During the integration period, any pixel containing freshly formed ice, even if that pixel previously contained multi-year ice, was declared first-year ice with a thickness of 0.75 meters and an initial Chl *a* concentration of 1 mg m^{-3}.

Maps of snow distribution and thickness required by the model were generated every day using passive microwave imagery from the SSM/I [*Arrigo et al.*, 1996]. The mean value for snow thickness (h_S) estimated from SSM/I data was nearly identical to that calculated from >1400 in situ measurements obtained in the Weddell Sea (0.17 m) during 1986, 1989, and 1992 (Figure 3). *Wadhams et al.* [1987] reported average snow thickness in the eastern Weddell Sea of approximately 0.11 m, about 35% lower than the average for the rest of the Weddell Sea. This is consistent with snow depths over the sea ice calculated from SSM/I data which indicate that snow cover is lowest in the eastern Weddell Sea in November (Plate 1). Snow thickness generated for the full 625 km^2 SSM/I pixel exhibited a normal, rather than a lognormal distribution, due to the larger spatial scales over which the data was being averaged, although the mean remained unchanged. The differences in the two distributions is not surprising, however. The Central Limit Theorem states that the sampling distribution of the mean approaches the normal distribution as the sample size increases, regardless of the shape of the distribution
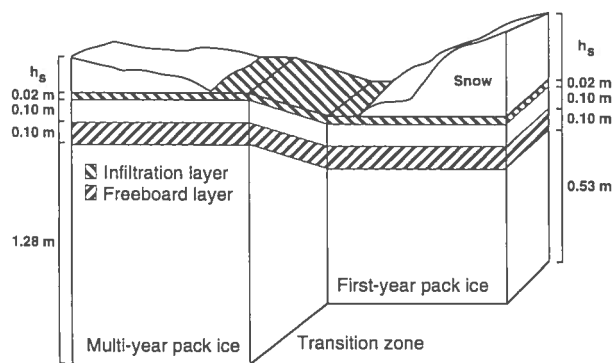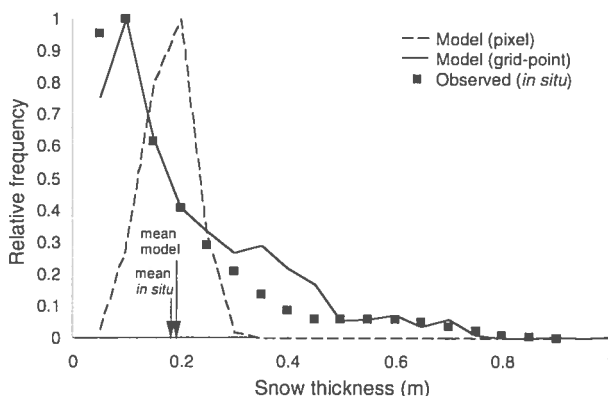

Fig. 2. A schematic illustration of the pack ice ecosystem as defined in the model. The ice pack consists of first-year and multi-year sea ice at a thickness of 0.75 and 1.50 m, respectively, with a narrow transition zone in between. Only the thickness of the lower layer differs among the different ice types. All ice types have a variable thickness snow cover (*hs*), an infiltration layer and an internal freeboard layer. Algae only grow within the infiltration and the freeboard layer. Brine volume and ice permeability change as a function of temperature. Nutrient flux is a function of whether the ice surface is flooded (a function of ice thickness and snow mass) and the sea ice permeability.
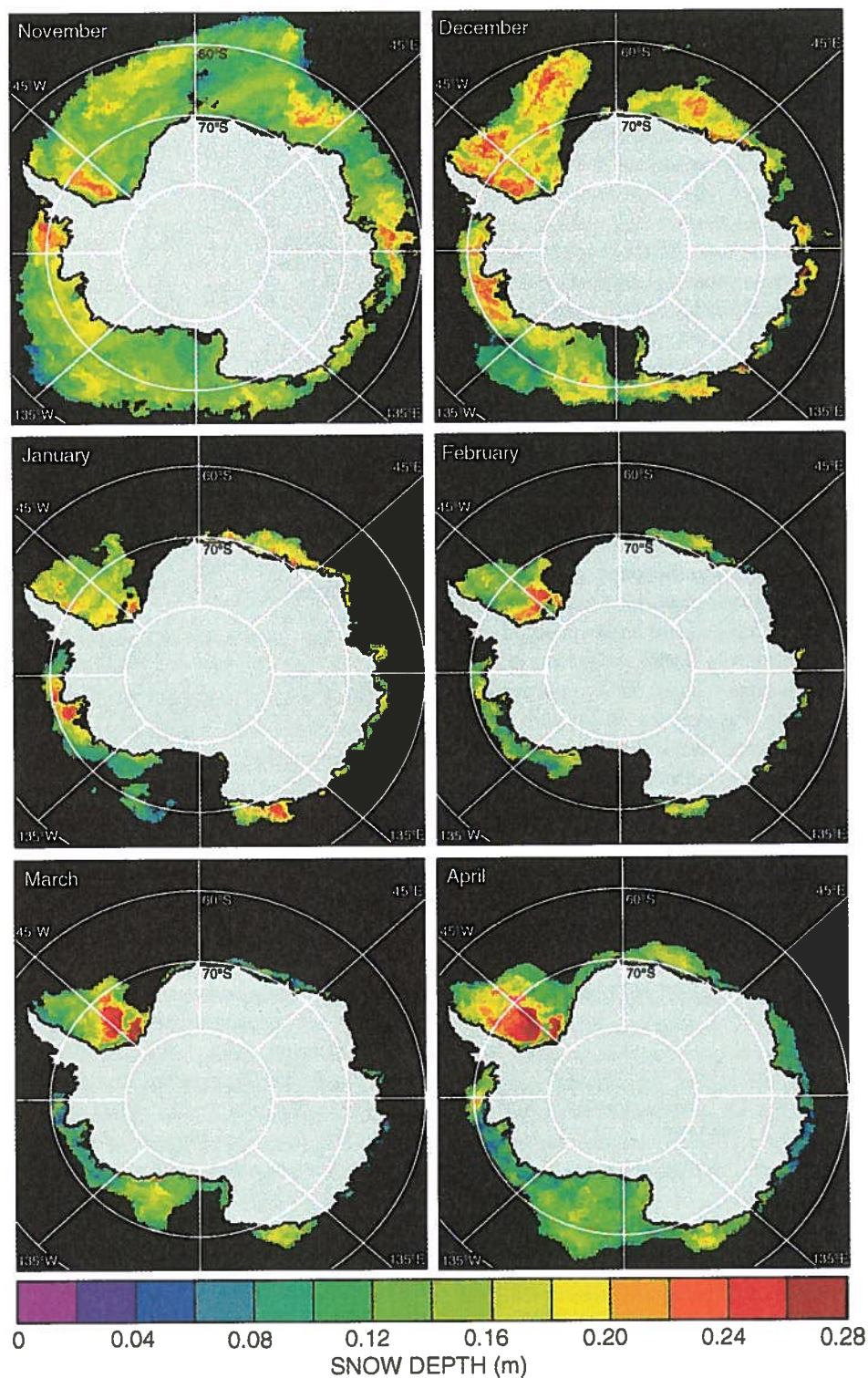
Plate 1. Sea ice distribution and snow thickness in the Weddell Sea in 1989-90. Sea ice extent is shown as colored pixels. Black pixels represent open water, gray pixels are land or semi-permanent ice shelves.

of the raw data. In our case, the SSM/I averages the snow depth over an area of 625 km², which is essentially the same as increasing the sample size, resulting in a normal distribution. Despite the differences in distribution, the agreement between the means of the two data sets suggests that the algorithm provides a reasonable estimate of h_S from SSM/I satellite data over a large area.

Horizontal variability of snow thickness within a 625 km² SSM/I pixel is substantial. Therefore, sub-pixel variation in snow thickness was simulated by creating nine equal area grid points per pixel. The snow thickness at each grid point was calculated by multiplying the snow depth for that pixel by one of nine multipliers. These multipliers (0.272, 0.532, 0.952, 1.74, 3.308, 1.305, 0.721, 0.427, 0.102) were chosen so that the distribution of snow thickness within each 625 km² pixel was consistent with the lognormal frequency distribution observed in situ (Figure 3). To simulate temporal changes in show thickness at each grid point, every 4 days the multiplier applied to each grid point was randomly shifted at most one position to the right or left (1/3 of the time no shift was made) of the previous multiplier in the array above. The array was ordered such that the difference between adjacent elements was minimized, ensuring that temporal changes in snow thickness at each grid point were not too abrupt. For example (Figure 4), after a multiplier of 0.721 had been applied to a grid point, the potential multipliers which could be applied subsequently are 1.305, 0.721, or 0.427, with the actual multiplier chosen at random. Production was calculated independently for each grid point and all grid points within a pixel were averaged to obtain the productivity for that pixel.

In the infiltration layer, nutrients were assumed to be equivalent to seawater concentrations when the snow density and snow thickness were sufficient to force the sea ice below sea level (the ice surface became flooded). The amount of snow needed to submerge the ice sheet was calculated as

$$hs_{crit} = (hs + H)\frac{(\rho_w - \rho_i)}{\rho_s} \qquad (1)$$

where h_s and H are snow and sea ice thickness (m), respectively, and ρ_i, ρ_w, and ρ_s are the densities of sea ice, seawater (1.028 g cm⁻³), and snow, respectively. When the daily air temperature was above freezing, the density of wet snow (0.6 g cm⁻³) was used; for dry snow, a density of 0.4 g cm⁻³ was used. The density of sea ice was calculated daily from the brine salinity and brine density [*Arrigo et al.*, 1993].

Day t, $\overline{h_s}$ = 0.17 m			Day t+1, $\overline{h_s}$ = 0.19 m		
grid point 1	grid point 2	grid point 3	grid point 1	grid point 2	grid point 3
multiplier 0.272	0.532	0.952	0.272	0.532	0.952
h_s 0.046	0.090	0.161	0.052	0.101	0.181
grid point 4	grid point 5	grid point 6	grid point 4	grid point 5	grid point 6
multiplier 1.74	3.31	1.31	1.74	3.31	1.31
h_s 0.296	0.562	0.221	0.331	0.629	0.249
grid point 7	grid point 8	grid point 9	grid point 7	grid point 8	grid point 9
multiplier 0.721	0.427	0.102	0.721	0.427	0.102
h_s 0.123	0.073	0.017	0.136	0.081	0.019

Day t+4, $\overline{h_s}$ = 0.22 m			Day t+8, $\overline{h_s}$ = 0.20 m		
grid point 1	grid point 2	grid point 3	grid point 1	grid point 2	grid point 3
multiplier 0.102	0.272	0.532	0.102	0.272	0.532
h_s 0.022	0.060	0.117	0.020	0.054	0.106
grid point 4	grid point 5	grid point 6	grid point 4	grid point 5	grid point 6
multiplier 0.952	1.74	3.31	0.952	1.74	3.31
h_s 0.209	0.383	0.728	0.190	0.348	0.662
grid point 7	grid point 8	grid point 9	grid point 7	grid point 8	grid point 9
multiplier 1.31	0.721	0.427	1.31	0.721	0.427
h_s 0.288	0.159	0.094	0.262	0.144	0.085

Fig. 4. An example of how sub-pixel variation in snow thickness was simulated within each pixel in the model. Because the variation in snow depth within a 625 km² area is expected to be considerable, each pixel was subdivided into 9 grid points in the model to incorporate spatial variation. Each grid point was assigned a multiplier such that when each is multiplied by the average snow depth (determined by the snow thickness algorithm) for that pixel, the frequency distribution of snow depths within each pixel approximates the distribution in situ. Panel A shows the snow depth (the product of the multiplier and the average snow depth) for each grid point on Day t when the average snow depth for that pixel is 0.17 m. Every four days, the multipliers may be shifted one grid point to the left (-1), not at all (0), or one grid point to the right (+1); the choice is made at random. On Day t+1 (panel B), no shift has yet been made and the change in snow depth at each grid point is due only to the change in the average snow depth for that pixel as determined by the snow thickness algorithm. By Day t+4 (panel C), the multipliers have shifted one step to the right (+1) and the snow depth for each grid point are adjusted accordingly. Four days later on Day t+8 (panel D), the multipliers did not shift (0 was chosen) and the changes in snow depths at each grid point were again only a function of changes in the average snow depth.

In the freeboard layer, when either the surface flooded or the brine volume exceeded 70 ‰ nutrients were scaled to the seawater concentrations according to

$$[N_{ii}] = [N_{iw}]\frac{S_b}{S_w} \qquad (2)$$

where $[N_{ii}]$ and $[N_{iw}]$ are the concentrations of nutrient i in the ice and seawater, respectively, S_b is the brine sa-

linity, and S_w is the seawater salinity. Spatial variation in nutrient concentrations within seawater, which supplies the sea ice, were obtained from annual climatologies [*Conkright et al.*, 1994]. Monthly climatological seawater salinity was obtained from *Levitus et al.* [1994] and interpolated daily.

If the individual criteria for the infiltration and freeboard layer were not met, ice algae within these layers were forced to survive on residual nutrients until the surface flooded or the ice became permeable again. During this time, changes in nutrient concentration at depth z were calculated solely as a function of algal demand, such that

$$\frac{dN_i}{dt}(z) = G(z)M(z)\frac{N_i}{C} \qquad (3)$$

where N_i is the concentration of nutrient i (either nitrate, silicic acid, or phosphate) $G(z)$ is the algal growth rate (d^{-1}) at depth z, $M(z)$ (mg C m^{-3}) is the algal standing crop at depth z, and N_i/C is the Redfield ratio of cellular nutrient i to cellular carbon (g:g).

The rate of change of M at depth z was calculated as

$$\frac{\partial M}{\partial t}(z) = [G(z) - L] \bullet M(z) \qquad (4)$$

where L is the specific microalgal loss rate (d^{-1}). Algal loss terms include death, sinking, and grazing by microzooplankton. Unfortunately, rates of algal sinking and zooplankton grazing are not well understood for pack ice communities. Therefore, a generalized specific loss has been applied in the model.

When considered together, the independent effects of temperature, salinity, and resource limitation act multiplicatively [*Arrigo and Sullivan*, 1994]. Therefore, algal growth can be defined as

$$G(z) = G_{max}(z)\, r_{lim}(z)\, S_g(z) \qquad (5)$$

where G_{max} (d^{-1}) is the maximum temperature specific microalgal net growth rate, r_{lim} is a dimensionless term which quantifies resource limitation (light or nutrients), and S_g (dimensionless) describes the dependence of algal growth on salinity.

The non-limited temperature dependent growth rate, G_{max}, is computed from [*Eppley et al.*, 1972]

$$G_{max}(z) = G_O \exp[r_G T(z)] \qquad (6)$$

where G_O (d^{-1}) is the specific growth rate at 0° C, r_G (°C^{-1}) is a rate constant which determines the sensitivity

of G_{max} to changes in temperature, and T (°C) is temperature (Figure 5A). *Eppley et al.* [1972] determine G_O and r_G to be 0.8511 d^{-1} and 0.0633 °C^{-1}, respectively, based on the growth of a variety of phytoplankton species acclimated to temperatures above 2 °C. This formulation also appears to adequately describe algal growth at lower temperatures [*Grossi et al.*, 1984; *Spies*, 1987; *Robinson*, 1992].

The rate of algal growth is determined in part by the availability of a single most limiting resource [*Blackman*, 1905]. Therefore, the maximum specific growth rate is reduced by the resource limitation term, r_{lim}, which is determined by the amount of either light or nutrients at a given depth, whichever was most limiting

$$r_{lim}(z) = \text{MINIMUM } [N_{lim}(z), \rho(z)] \qquad ($$

where $r_{lim}(z)$ is equivalent to the smaller of the nutrient limitation term, $N_{lim}(z)$, and the light limitation term $\rho(z)$.

The empirical formulation of *Monod* [1942] has been modified to quantify the limitation imposed by the available concentration of each nutrient (in this case either nitrate or silicate) such that

$$\left(\frac{G}{G_{max}}\right)_i(z) = \frac{N_i(z)}{K_s + N_i(z)} \qquad ($$

where $(G/G_{max})_i$ describes the fraction of the maximum temperature-dependent growth rate allowed by N_i (at depth z, and K_s is the half-saturation constant for N_i (and is 60 μM for silicate and 0.5 μM for nitrate) defined as the concentration where $G = 0.5\, G_{max}$ (Figure 5B). Determination of $N_{lim}(z)$ is made by evaluating Eq. 8 for each nutrient such that

$$N_{lim}(z) = \text{MINIMUM}\left(\frac{G}{G_{max}}\right)_i(z).$$

Light limitation is calculated as

$$\rho(z) = 1 - \exp\left(-\frac{PUR(z)}{I_k'(z)}\right) \qquad ($$

where PUR is the amount of photosynthetically usable radiation [*Morel*, 1978] and I_k' is the spectral photoadaptation parameter as determined from Figure (additional details are available in *Arrigo and Sullivan* 1994).

Finally, the effects of sub- and supra-optimal salinity on sea ice algal growth were also included [*Arrigo et al.* 1992). At thermal equilibrium, the salinity of sea ice brine (S_b) is determined directly by temperature; t
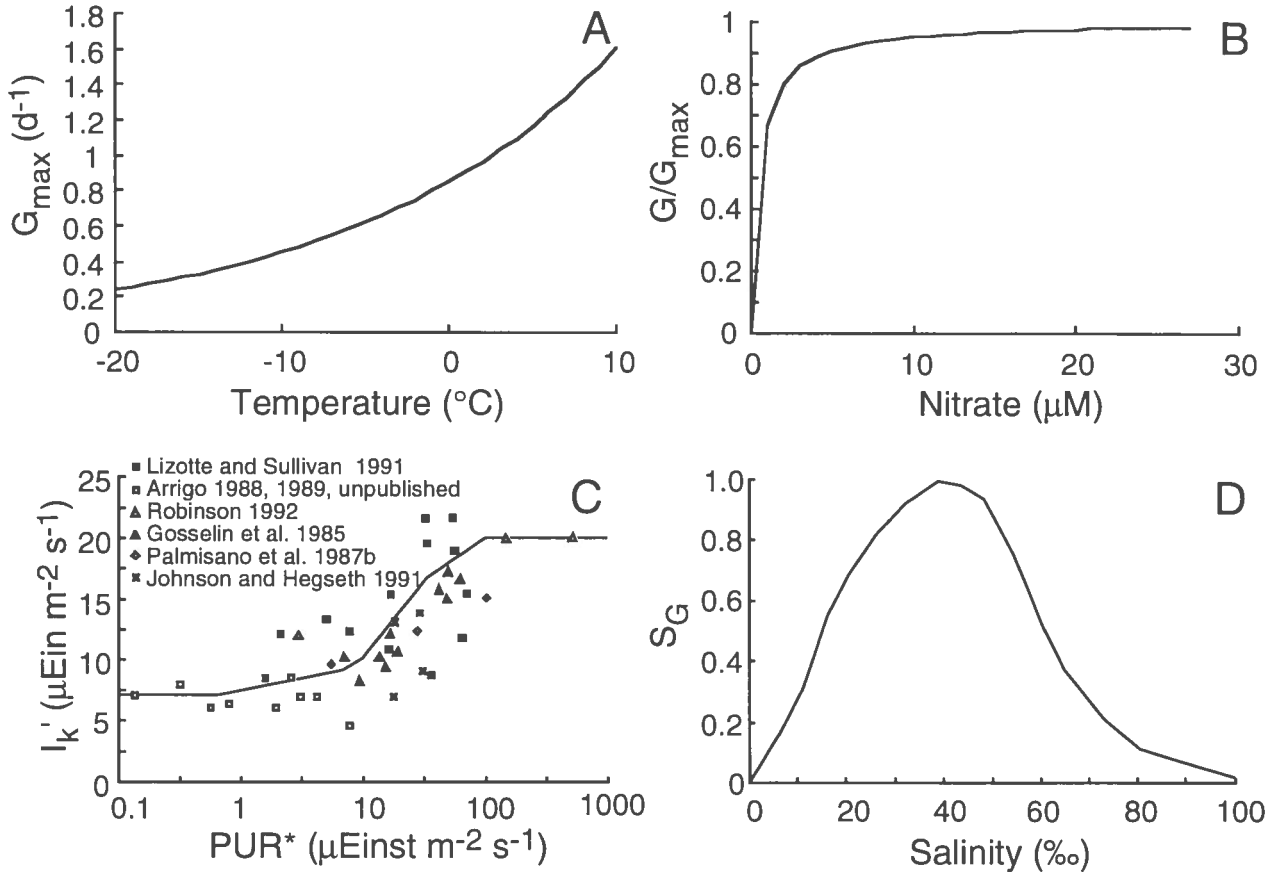
Fig. 5. The relationship between algal growth and (*a*) temperature (see Eq. 6), (*b*) nitrate concentration (see Eq. 8, silicate is not shown here), (*c*) light availability (see Eq. 10), and (*d*) brine salinity (see Eq. 11) used in the model.

colder temperatures at the upper sea ice surface result in higher S_b values. Salinity can have a substantial impact on rates of algal photosynthesis and growth [*Grant and Horner*, 1976; *Arrigo and Sullivan*, 1992) and appears to act independently of both temperature and resource limitation [*Arrigo and Sullivan*, 1992]. The salinity-dependent growth coefficient, $S_g(z)$, at a given depth was determined by the least-squares polynomial fit to the data; this fit is shown in Figure 5D

$$S_g(z) = \alpha_0 + \alpha_1 S_g(z) + \alpha_2 S_g(z)^2 + \alpha_3 S_g(z)^3 \quad (11)$$

where $S_g(z)$ is the brine salinity, $\alpha_0 = -1.2073 \times 10^1$, $\alpha_1 = 7.097 \times 10^{-2}$, $\alpha_2 = -1.33 \times 10^{-3}$, and $\alpha_3 = 6.342 \times 10^{-6}$.

The transmission of downwelling spectral irradiance through the snow and ice sheet was estimated as described in *Arrigo et al.* [1994]. Cloud cover, relative humidity, and sea level pressure and air temperature used in the atmospheric model of *Gregg and Carder* [1990] were obtained from *da Silva et al.* [1994]. Total column

ozone used by the *Gregg and Carder* [1990] model was calculated as the averaged monthly climatologies from years 1989-1991 of the TOMS data. Total column precipitable water was calculated as the averaged monthly climatological data from Tiros Operational Vertical Sounder (TOVS) for the years 1985-1988. The monthly climatologies were interpolated daily during the model integration.

3. RESULTS AND DISCUSSION

3.1. *Evaluation of model performance and algal losses*

Because the Weddell Sea has been the most extensively studied ice covered region in the Antarctic, this site was useful for testing the performance of the model and determining an appropriate value for *L*. The mean monthly ice algal standing crop for the Weddell Sea was calculated from biomass data provided by 257 ice cores collected at a variety of times and locations throughout

TABLE 1. Comparison of Sea Ice Extent and Productivity Within the Antarctic Ice Pack.

Ice Type	Sea Ice Extent (10^6 km^2)			Productivity (g C m^{-2} month^{-1})	Productivity (Tg C month^{-1})		
	First-year	Multi-year	All ice	All ice	First-year	Multi-year	All ice
Weddell Sea							
October	4.89	0.95	5.85	0.20	1.16	0.03	1.19
November	4.17	0.92	5.09	0.90	4.26	0.34	4.60
December	2.06	0.90	2.96	1.44	3.49	0.78	4.26
January	0.66	0.84	1.51	1.89	1.90	0.94	2.84
February	0.40	0.76	1.16	1.33	0.82	0.73	1.54
March	0.63	0.73	1.35	0.73	0.49	0.49	0.98
April	1.36	0.72	2.08	0.18	0.21	0.16	0.37
Annual production (Tg C)							15.79
Bellingshausen-Amundsen Seas							
October	1.37	0.47	1.85	0.09	0.15	0.01	0.17
November	1.19	0.46	1.65	0.64	0.93	0.12	1.06
December	0.52	0.44	0.96	0.95	0.58	0.33	0.91
January	0.25	0.40	0.64	0.99	0.27	0.36	0.64
February	0.12	0.30	0.42	0.85	0.09	0.26	0.36
March	0.20	0.24	0.44	0.60	0.04	0.23	0.26
April	0.44	0.23	0.67	0.29	0.03	0.16	0.20
Annual production (Tg C)							3.59
Ross Sea							
October	3.06	0.87	3.94	0.21	0.74	0.10	0.84
November	2.34	0.86	3.20	0.78	2.23	0.27	2.49
December	1.45	0.71	2.16	1.24	2.01	0.67	2.68
January	0.37	0.37	0.74	1.24	0.52	0.39	0.91
February	0.11	0.27	0.37	0.81	0.05	0.26	0.30
March	0.75	0.22	0.97	0.27	0.08	0.18	0.26
April	1.95	0.22	2.17	0.11	0.11	0.13	0.23
Annual production (Tg C)							7.73
Western South Pacific Ocean							
October	0.60	0.41	1.01	0.11	0.07	0.04	0.11
November	0.55	0.37	0.91	0.64	0.35	0.24	0.58
December	0.23	0.26	0.49	0.86	0.15	0.27	0.42
January	0.14	0.20	0.34	0.95	0.11	0.22	0.32
February	0.08	0.14	0.22	0.87	0.04	0.15	0.19
March	0.22	0.10	0.32	0.50	0.05	0.11	0.16
April	0.59	0.09	0.68	0.20	0.07	0.06	0.13
Annual production (Tg C)							1.92

TABLE 1 (continued)

Ice Type	Sea Ice Extent (10^6 km^2)			Productivity (g C m^{-2} month^{-1})	Productivity (Tg C month^{-1})		
	First-year	Multi-year	All ice	All ice	First-year	Multi-year	All ice
South Indian Ocean							
October	3.45	0.25	3.70	0.19	0.65	0.05	0.70
November	2.55	0.24	2.79	0.99	2.56	0.21	2.76
December	0.94	0.19	1.13	1.35	1.31	0.21	1.53
January	0.33	0.15	0.48	1.93	0.74	0.18	0.92
February	0.16	0.11	0.26	1.60	0.29	0.13	0.42
March	0.16	0.07	0.23	0.84	0.10	0.09	0.19
April	0.57	0.05	0.62	0.21	0.07	0.06	0.13
Annual production (Tg C)							6.66
SOUTHERN OCEAN TOTAL							
October	13.4	2.96	16.3	0.18	2.78	0.23	3.01
November	10.8	2.84	13.6	0.84	10.3	1.17	11.5
December	5.19	2.50	7.69	1.28	7.55	2.26	9.80
January	1.75	1.96	3.71	1.52	3.54	2.10	5.64
February	0.87	1.57	2.43	1.15	1.29	1.52	2.81
March	1.97	1.35	3.31	0.56	0.76	1.09	1.86
April	4.90	1.32	6.22	0.17	0.49	0.57	1.06
Annual production (Tg C)				26.7	8.95		35.7

the region (see *Dieckmann et al.*, this volume). The time series generated from this information agreed remarkably well with model predictions when $L=0.03$ d^{-1} (Figure 6A). The standard deviation of the monthly mean standing crop estimates resulting from both the temporal variation within each month and the spatial variability within the Weddell Sea were also very similar in magnitude, in both cases being approximately equal to the monthly means. Manipulating the value for L, for which very little data is available, only changed the height of the curve shown in Figure 6A, it did not change its shape. The temporal trends in algal standing crop, which peaked in January and February, depended upon other aspects of the model.

The accuracy of the model is further demonstrated by comparing the predicted frequency distributions of algal standing crops in the Weddell Sea to values determined from ice cores (Figure 6B). In both cases, algal standing crops in the range of 0-5 mg Chl *a* m^{-2} were most plentiful, with a rapid decline in frequency of values >5 mg

Chl *a* m^{-2}. Both also exhibited a substantial number of locations where standing crops range from 5 to 30 mg Chl *a* m^{-2}. Standing crops greater than 40 mg Chl *a* m^{-2} were rare in both the model run and in collected ice cores. These results suggest that our simplified physical model captured the essential features of the complex pack ice ecosystem and should provide reasonable estimates of algal production.

3.2. *Productivity of the Antarctic ice pack*

The annual rate of primary production within Antarctic sea ice was calculated to be approximately 35.7 Tg C, consistent with previous estimates which range from 30 Tg C [Mathot et al., 1996] to 70 Tg C [*Legendre et al.*, 1992]. Total primary production in Antarctic sea ice was a function of both the sea ice extent and the rate of carbon fixation per unit surface area (Table 1). Although sea ice was at its maximum extent in October, because of low production rates during this time, spatially integrated
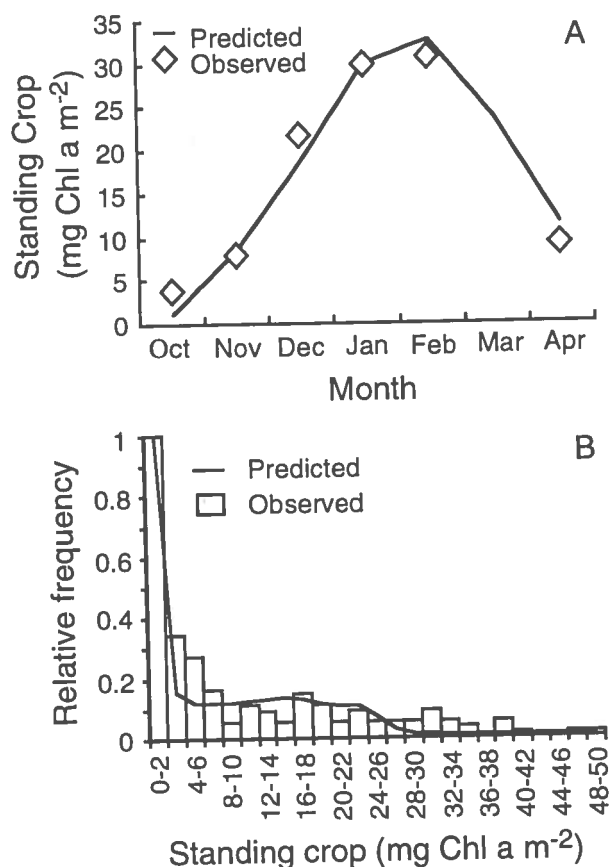
Fig. 6. Results of model validation studies for the Weddell Sea region. A loss rate of 0.03 d^{-1} was found to produce superior results in terms of (a) mean monthly standing crop and (b) relative frequency distribution microalgal standing crop.

in coverage again during March and April, the low productivity rates in this newly formed sea ice resulted in a lower amount of production than in the established multi-year ice.

Estimates of annual primary production in the Southern Ocean have been made for both phytoplankton and sea ice microalgae over the past 30 years, with values varying widely as new information becomes available and our understanding of Southern Ocean ecology improves. Early estimates of annual phytoplankton production made by *Ryther* [1963] and *Bunt* [1968] ranged from 6 to 130 g C m^{-2} yr^{-1}, and total production in the Southern Ocean was estimated to be 3,000 Tg C yr^{-1}. However, the available data for these values were primarily for high-productivity waters on the continental shelves. Estimates dropped 80% to 600 Tg C yr^{-1} as the number of measurements in pelagic waters under nonbloom conditions increased [*Holm-Hansen et al.*, 1977; *El Sayed*, 1978]. Recognition of phytoplankton bloom formation in the marginal ice zone led to arguments that another 140-400 Tg C yr^{-1} should be added [*Smith and Nelson*, 1986; *Legendre et al.*, 1992], bringing estimates of Southern Ocean phytoplankton production to 740-1000 Tg C yr^{-1}.

Much less attention has been paid to measurements of primary production in sea ice, which appears to be the unfortunate result of early, low estimates. Measurements made in near-shore sea ice led to estimates on the order of 1 to 6 g C m^{-2} yr^{-1} [*Burkholder and Mandelli*, 1965; *Bunt and Lee*, 1970]. Given that these estimates were orders of magnitude lower than those being reported for phytoplankton, the contribution of primary production in sea ice was dismissed as insignificant [*Bunt*, 1968; *Fogg*, 1977]. This conventional wisdom persisted until it was demonstrated that sea ice algal productivity in McMurdo Sound was more than ten-fold higher than rates reported previously [*Grossi et al.*, 1987; *Arrigo et al.*, 1993b]. Studies of pack ice in the pelagic ocean confirmed the need to revisit the question of whether sea ice algae make a significant contribution to the Southern Ocean carbon cycle [e.g., *Ackley et al.*, 1979; *Lizotte and Sullivan*, 1991, 1992]. A recent estimate for Antarctic sea ice algae put the annual primary production at 63 to 70 Tg C yr^{-1} [*Legendre et al.*, 1992], or 6 to 10% of the value estimated for Southern Ocean phytoplankton.

Our production rate of 35.7 Tg C yr^{-1} for Antarctic sea ice is about 4% of the annual biogenic carbon production in the Southern Ocean. However, sea ice primary production is a much larger fraction (10-28%) of total production in the ice covered Southern Ocean, which ranges from 141 to 383 Tg C year^{-1} [*Legendre et*

rates of production were depressed (3.89 Tg C month^{-1}). Primary production in Antarctic sea ice was greatest in November (12.96 Tg C month^{-1}) as areal rates of production increased by a factor of four (Plate 2) and sea ice coverage remained high. Over 90% of this biogenic carbon was produced within first-year sea ice. Approximately 60% of annual production occurred during the months of November and December. Spatially integrated production declined between December and April, due to the dramatic decrease in first-year sea ice coverage (Plate 1). The rate of production per unit area peaked in January in both first-year (2.17 g C m^{-2} month^{-1}) and multi-year sea ice (1.09 g C m^{-2} month^{-1}), respectively. In February, spatially averaged rates of production in first-year sea ice exceeded those in multi-year ice; however, due to the continued melting of first-year sea ice, the bulk of the biogenic carbon was being produced in multi-year ice. Although first-year sea ice increased

al, 1992; *Smith and Nelson*, 1986] and includes the highly productive marginal ice zones. Furthermore, it is likely that the 35.7 Tg C yr^{-1} we estimated for surface ice communities is an underestimate of total production in the Antarctic ice pack due to the simplifying assumptions made when constructing the model.

First, it was assumed in the model that the ice pack consisted of a single continuous sheet. However, the pack is often made up of individual floes and contains numerous leads and fissures which would increase both the surface area for algal colonization and the transmittance of light through the snow and ice sheet [*Lizotte and Arrigo*, 1992]. This would result in higher growth rates than those predicted by the model. Similarly, the model excludes features such as pressure ridges and rafted ice floes which increase the ice thickness and facilitate snow accumulation [*Eicken et al.*, 1994]. It has also been suggested that aeolian erosion of the snow trapped in pressure ridges creates a conduit for light to be transmitted to the ice interior, thus promoting ice algal growth [*Smetacek et al.*, 1990, *Eicken et al.*, 1994].

Second, because the distribution of land-fast ice and/or underlying platelet ice is largely unknown for the Weddell Sea region, these ice types were excluded from the model. It has been shown that rates of productivity within land-fast and platelet ice can be more than an order of magnitude higher than those reported in pack ice [*Grossi et al.*, 1987; *Arrigo et al.*, 1994]. Therefore, because Antarctic sea ice consists of approximately 1-2% land-fast ice [*Legendre et al.*, 1992], including these regions would increase estimates of productivity substantially [*Ackley and Sullivan*, 1994].

Third, the model neglects bottom ice and internal algal communities (except for the freeboard layer) since it is thought that due to low nutrient fluxes, productivity in these internal bands is very low [*Legendre et al.*, 1992]. There are, however, a number of processes that can drive nutrient exchange between the interior of the ice and the underlying water column, and which may enhance production within internal bands. As the sea ice thaws in spring and summer, its brine volume increases substantially and the pack becomes quite porous, enabling seawater to infiltrate the interior from the top, bottom, and in areas near the edge of a flow, from the sides [*Ackley and Sullivan*, 1994]. In addition, in late summer and autumn, refreezing of the upper ice pack produces high salinity brines which flow out of the pack. This process drives convection-like currents which bring seawater and a fresh supply of nutrients into the ice interior [*Fritsen et al.*, 1994, Fritsen et al. this volume]. These processes are complex and difficult to describe quantitatively and have not yet been incorporated into the model.

Finally, the model domain only included those locations where the sea ice concentration determined from SSM/I exceeded 50%. Although this results in a slight underestimate of the area of the ice pack, it was a necessary restriction because the performance of snow thickness algorithm degrades in the presence of large amounts of open water.

3.3. *Weddell Sea (60°W to 20°E)*

The sea ice cover was most extensive in the Weddell Sea sector of the Antarctic ice pack, in terms of both first-year and multi-year sea ice (Plate 1). This provided the ice algae a relatively large substrate on which to grow and should be kept in mind when total production estimates of the different Antarctic sectors are compared. The coverage of first-year ice peaked in October at approximately 4.9×10^6 km^2 (Table 1), with the sea ice extending as far north as 60°S. By February, only 0.4×10^6 km^2 of the first-year sea ice remained. Coverage of multi-year ice was much less extensive but also less variable, ranging from 0.95×10^6 km^2 in October to 0.72×10^6 km^2 in April. Multi-year ice in the Weddell Sea was restricted to the western margin along the Antarctic Peninsula.

The mean snow thickness in the Weddell Sea was 0.16 m, about 20% greater than that of the other Antarctic sectors (0.14 m). Although this difference may seem to be too small to be of consequence, it results from the Weddell Sea having 2 to 7 times more area with snow thickness >0.2 m than the other Antarctic sectors.

Rates of primary production in the Weddell Sea exceeded those in all other Antarctic sectors. At numerous locations, the rate of primary production was >100 mg C m^{-2} d^{-1} (Plate 2). The most productive region of the Weddell Sea, and indeed of the entire Antarctic ice pack, was located within the first-year ice (near the eastern margin of the perennial ice) along 45°W. Here the snow remained relatively deep for the duration of the simulation. This thick snow cover frequently forced the ice sheet below sea level, resulting surface flooding and providing nutrients to the algal communities, which attained high standing crops (Plate 3). Although the deep snow also reduced light availability, the average snow depth within the bloom was insufficient to seriously inhibit the algal growth, except in multi-year ice.

Nearly 50% of annual Antarctic sea ice primary production (15.8 Tg C) was generated in the Weddell Sea (Table 1) due to its extensive ice coverage and high rate
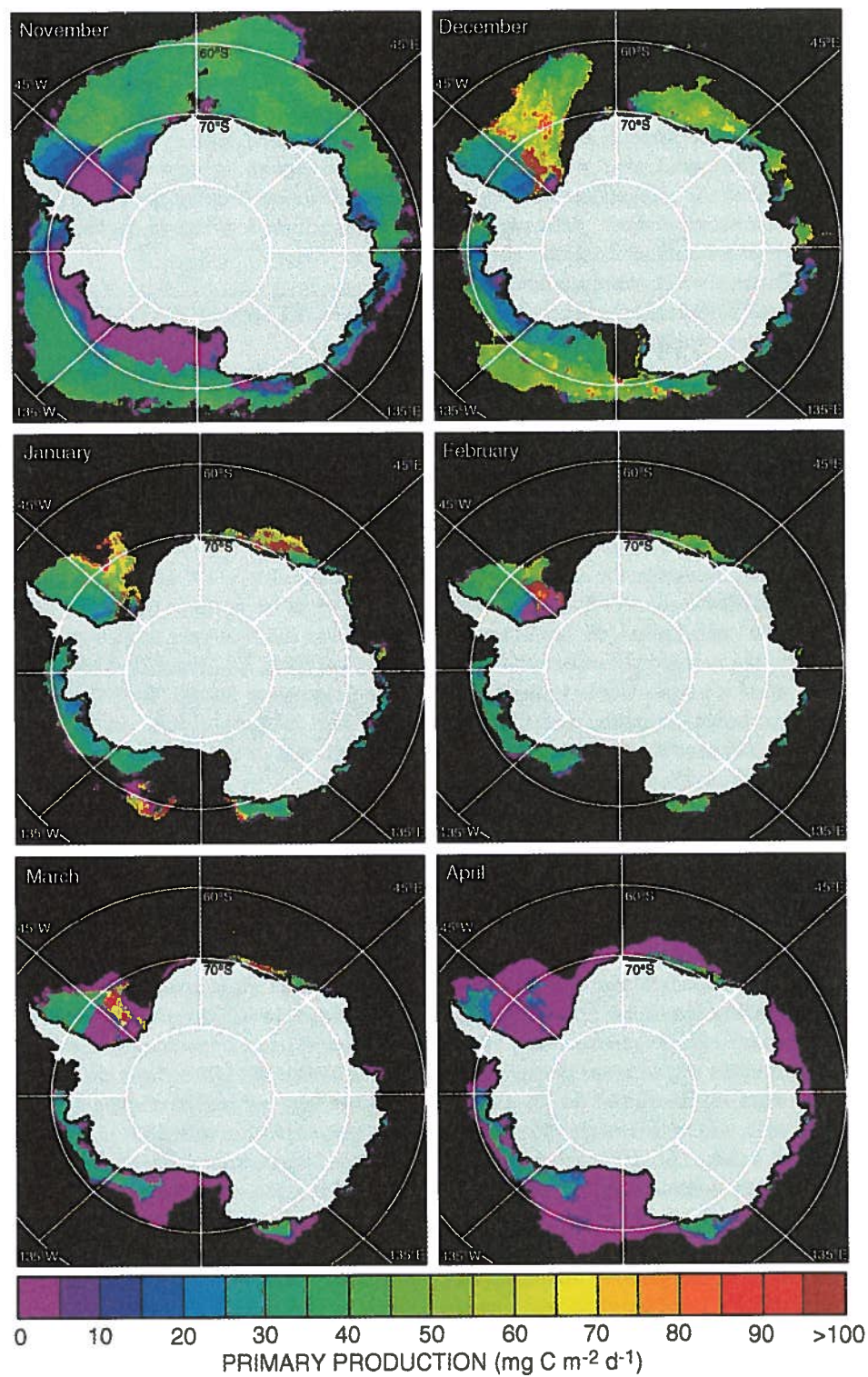
Plate 2. Temporal changes in simulated primary productivity for the Antarctic ice pack.
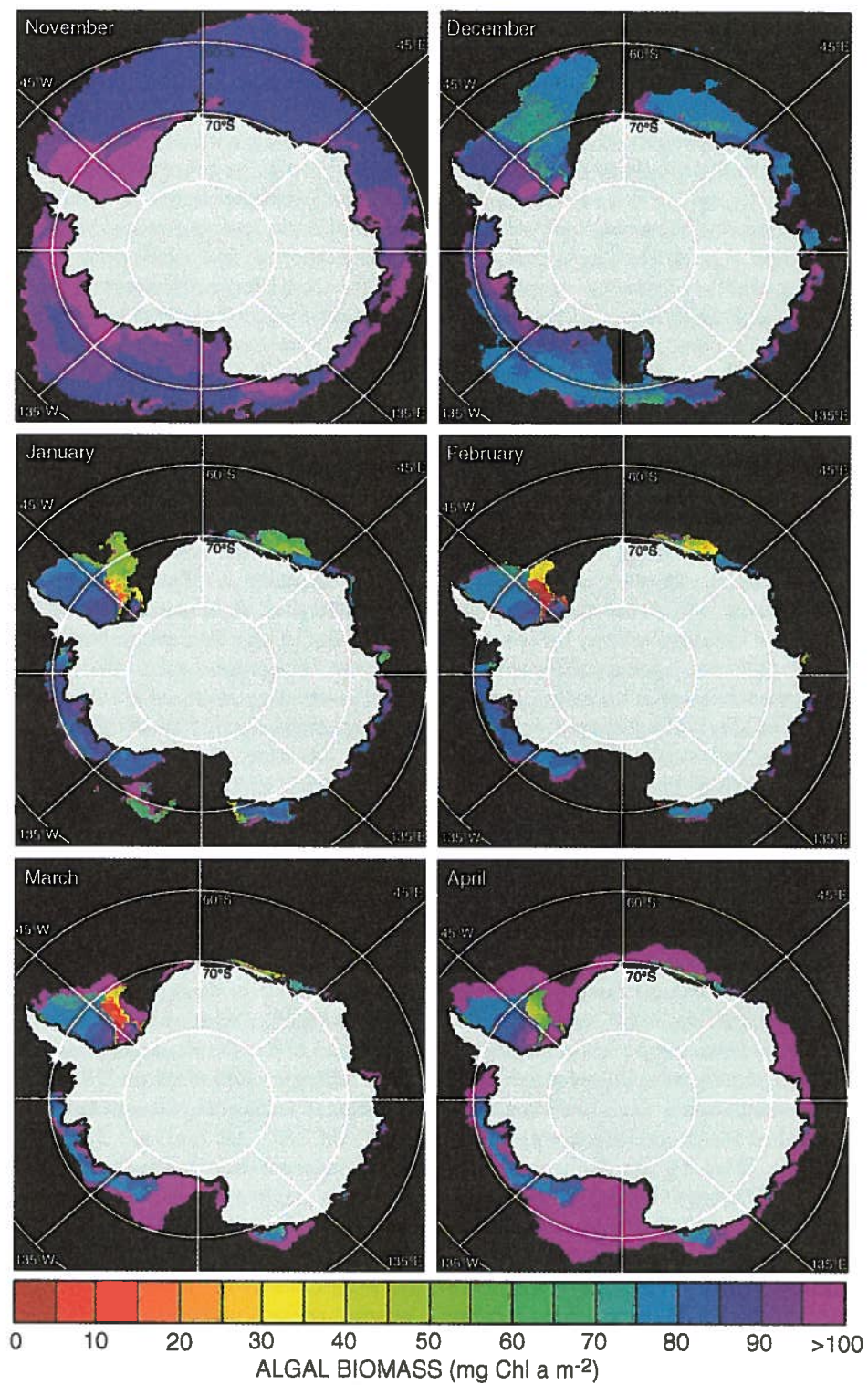
Plate 3. Temporal changes in simulated algal standing crop (Chl *a*) for the Antarctic ice pack.

of carbon fixation. The maximum rate of production per unit sea surface area in the Weddell Sea (2.86 g C m^{-2} month^{-1} in first-year ice in January) was more than twice as high as in the Ross Sea (1.42 g C m^{-2} month^{-1}). Annually, 74% (12.3 Tg C) of the sea ice production in the Weddell Sea took place within first-year ice; during the month of November first-year ice accounted for more than 93%. While sea ice was at its maximum extent in October, because of low algal growth rates during this time, spatially integrated rates of production were modest (1.19 Tg C month^{-1}). Primary production was greatest in November (4.60 Tg C month^{-1}) as areal rates of production increased by a factor of three and sea ice coverage remained high.

3.4. *Bellingshausen-Amundsen Sea (130°W to 60°W)*

Total sea ice coverage in the Bellingshausen-Amundsen Sea in 1989-90 was approximately 30% of that in the Weddell Sea (Plate 1, Table 1). However, a substantially larger fraction of total ice cover consisted of multi-year ice (25% in October to 71% in February). The snow thickness in the Bellingshausen-Amundsen Sea averaged 0.14 m, with the deepest snow (>0.25 m) located near the far eastern boundary of the Bellingshausen-Amundsen Sea (near the Antarctic Peninsula) in October and November. This peak in snow cover was short lived, however, as snow thickness declined markedly by December. From October through April, sea ice near the coast tended to have a thicker snow cover than ice offshore. Because multi-year ice is more prevalent near-shore, this is probably the result of long term accumulation.

The relatively thin snow cover over first-year ice in this region resulted in the infrequent flooding of the sea ice surface. The reduced nutrient supply in first-year ice and thick snow cover over multi-year ice produced generally low estimates of primary production for the sea ice in the Bellingshausen-Amundsen Sea. Only the South Pacific Ocean sector had lower spatially averaged rates of production (Plate 2, Table 1). Productivity in first-year ice was greatest in December (1.12 g C m^{-2} month^{-1}) and January (1.10 g C m^{-2} month^{-1}), but amounted to less than one half the rate in Weddell Sea first-year ice. Of the 3.59 Tg C fixed annually in the sea ice of the Bellingshausen-Amundsen Sea, 2.11 Tg, or 59%, was produced in first-year ice.

3.5. *Ross Sea (160°E to 130°W)*

Sea ice cover in the Ross Sea ranged from a maximum of 3.06 × 10^6 km^2 in October to 0.37 × 10^6 km^2 in February. Unlike other Antarctic sectors, the decay of the ice pack in the Ross Sea began over coastal waters with the formation of the Ross Sea polynya beginning in late November and December (Plate 1). The sea ice continued advecting north and eastward through January and February. A large concentration of multi-year ice (0.22 × 10^6 km^2) persisted in the far eastern portion of the Ross Sea adjacent to the Bellingshausen-Amundsen Sea. Snow cover was fairly uniform over the sea ice throughout the Ross Sea, particularly in the west where snow thickness ranged from 0.08 to 0.16 m. Only in the east did the snow cover exceed 0.20 m in thickness over a sizable area where it was primarily associated with the multi-year ice. A relatively thick snow cover was also apparent offshore during November in first-year ice located near 140°W.

The Ross Sea was the second most productive sector of the Antarctic ice pack (Plate 2, Table 1), due primarily to the extensive sea ice cover in November and December, contributing 7.7 Tg C annually. Between October and December, algal biomass in the Ross Sea was most abundant (15 mg Chl *a* m^{-2} in November and 30 mg Chl *a* m^{-2} in December) in the offshore sea ice where light levels were highest (Plate 3). Algal biomass near-shore was generally about 50% of the levels located offshore during this time. Most algal production took place in November (2.49 Tg C) and December (2.68 Tg), 74% of this production in first-year ice (Table 1). In January, the onshore-offshore differences in algal standing crop disappeared due to the melting of vast amounts of first-year sea ice; total sea ice extent had diminished dramatically to only approximately 10% of the coverage in October. Consequently, production dropped by 67% despite a peak in the rate of algal production per unit area (1.24 g C m^{-2} month^{-1}). Some multi-year ice at 160°E persisted to the end of the simulation and harbored the greatest algal standing crop in the Ross Sea, with levels in January occasionally exceeding 60 mg Chl *a* m^{-2}.

3.6. *Western South Pacific Ocean (90°E to 160 E)*

Because the western South Pacific sector is the least productive, contributing only 5% of total production or 1.92 Tg C annually (Table 1), it provides an interesting contrast to the highly productive Weddell Sea. The low productivity of the western South Pacific sector was due in part to the extremely limited sea ice area. Even during maximal ice coverage (1.01 × 10^6 km^2), the area of sea ice of this sector was only about 17% of that in the Weddell Sea, providing a much smaller habitat for algal growth.

Also responsible was the low productivity per unit area (maximum of 0.95 g C m^{-2} month^{-1} in January), which was <50% of the rate in the Weddell Sea. This low productivity was the result of a high proportion of multi-year sea ice and relatively thin snow over a relatively transient first-year ice cover. Between October and February, multi-year ice accounted for 40% to 64% of total sea ice cover, more than any other Antarctic sector. Snow depth in this sector was the thinnest of the Antarctic ice pack, averaging only 0.14 m. Consequently, a large fraction of the first-year ice in this sector remained above sea level and had restricted access to nutrients, resulting in ice algae experiencing substantial nutrient limitation.

3.7. *Southern Indian Ocean (20°E to 90°E)*

This sector had extensive sea ice coverage (3.45 × 10^6 km^2 in October), similar to that in the Ross Sea (Plate 2, Table 1), although the proportion of multi-year ice was somewhat less than in the Ross Sea. The most striking difference between this sector and the Ross Sea was the precipitous decline in ice coverage in December. Within one months time, sea ice coverage in the southern Indian Ocean was reduced to less than half of that in the Ross Sea.

The thickness of the snow cover was also strikingly similar to that in the Ross Sea, averaging 0.10 to 0.16 m. From the beginning of October through December, the thickest snow cover was concentrated in a region near 30°E, after which time the underlying sea ice disappeared (Plate 1). After December, the thickest snow cover was restricted to a relatively narrow band of multi-year ice adjacent to the coast.

Annual production in the southern Indian Ocean was approximately 14% less than in the Ross Sea, amounting to 6.66 Tg C. The difference was due in part to the smaller amount of production in December (1.53 Tg as compared to 2.68 Tg in the Ross Sea) which resulted from the greatly diminished sea ice coverage in the southern Indian Ocean (Table 1). In contrast, the rate of production per unit area was greater in the southern Indian Ocean due to the high proportion of first-year ice.

3.8. *Effects of snow thickness and sea ice type*

Model results demonstrate that the high degree of spatial and temporal variation in the magnitude of sea ice primary production shown above is largely a function of variations in snow depth which influence light attenuation and surface flooding. The relative impact of these two processes determines the magnitude of an ice algal bloom. In the Weddell Sea, the mean snow thickness was about 20% greater than that of the other Antarctic sectors and the fractional area covered by a layer of snow thicker than 0.2 m was much more extensive. Results of the model show that the infiltration community in the Weddell Sea benefited greatly from this thicker snow cover since the resulting surface flooding ensured a greater nutrient supply and higher growth rates. Although snow also reduced light availability, the average snow depth in the Weddell Sea was insufficient to seriously inhibit the algal growth, except in some multi-year ice areas.

The importance of snow cover in controlling rates of primary production can be seen clearly when temporal changes in both variables at a single location (38.40°W, 71.75°S) are plotted together (Figure 7). During the peak of the ice algal bloom (January-February), decreases in snow thickness almost always elicited a sharp drop in the rate of algal production. When algal biomass levels are elevated, nutrients in the infiltration and freeboard layer can be depleted rapidly when the nutrient supply becomes restricted. To maintain high rates of production requires continuous replenishment of nutrients which can only be achieved when snow is thick enough to cause surface flooding (the source of nutrients for the infiltration and freeboard layers) or if the brine volume is sufficiently high (>70 ‰) that the sea ice porosity allows free exchange of nutrients (an additional source of nutrients for the freeboard layer). When the snow cover thins, the ice pack floats higher in the water column and the nutrient supply to the infiltration and freeboard layer becomes restricted, resulting in a marked decrease in production.

Productivity and snow depth are only tightly coupled under conditions where nutrients are limiting (Figure 7). In the early stages of the simulation when biomass levels are low, changes in snow thickness had little effect on rates of production because nutrients were not depleted to the point of limiting algal growth. Near the end of the simulation, light levels decreased markedly and became the resource that limited algal production. Consequently, changes in snow thickness at that time had only a minor influence on algal productivity. Model results also illustrate the strong relationship between the fraction of multi-year sea ice within a region and the average rate of production per unit sea ice area. Multi-year ice frequently has a thick snow cover and very little light is able to penetrate to the depths of the algal layers. Plotting the percent multi-year ice versus the productivity per unit area (Figure 8), both averaged over the duration of
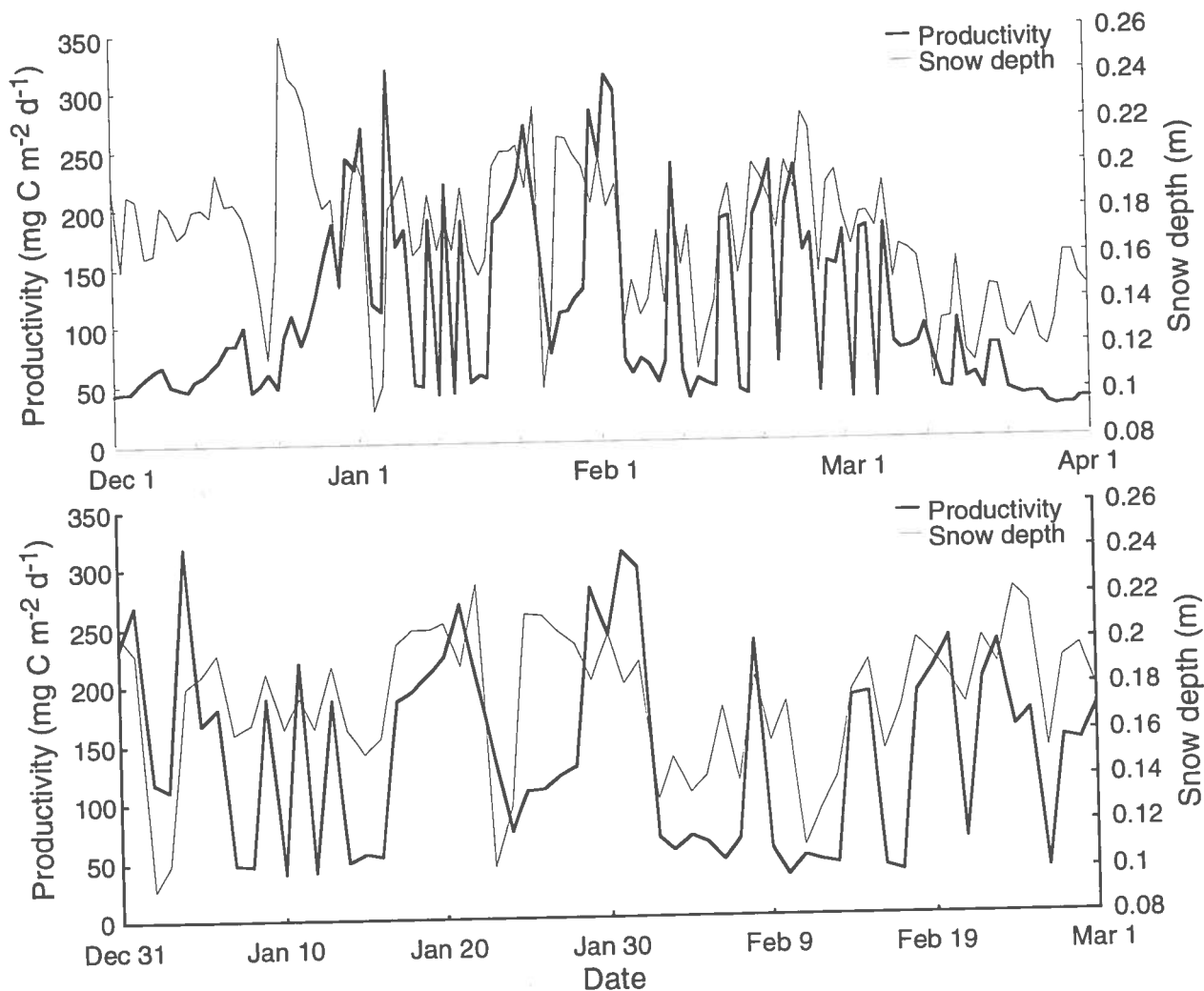
Fig. 7. The tight coupling between primary productivity and snow depth in the model during the period of maximum algal growth (January-February) at a single location in the annual ice of the Weddell Sea (38.40°W, 71.75°S). Coincident peaks and valleys reflect the fact that when biomass is high, algal growth is highly dependent on nutrient availability, which varies as changes in snow depth either submerge or elevate the ice surface. The bottom panel is the same as the top except that it extends over a shorter period of time so that more detail can be seen.

the simulation, demonstrates that as the percent multi-year ice declines so does the average productivity.

It is important that the amount of submerged ice area, as determined by the interaction of snow and ice thickness shown in Eq. 1, be estimated with reasonable accuracy in the model. *Wadhams et al.* [1987] drilled 4055 holes in the sea ice of the Weddell Sea and estimated that approximately 17.4% of the ice pack was submerged at any given time, ranging with latitude from 13.6% to 28.7%. In the model, 17.1% of the Weddell Sea ice pack (first- and multi-year ice) was below freeboard, with a temporal range of 9.39% to 25.1% (Figure 9), in excel-

lent agreement with in situ observations [*Wadhams et al.*, 1987]. The mean percent area below the freeboard was slightly higher for the Weddell Sea than for the entire Antarctic ice pack (15.3%) due to the thicker than average snow cover of the Weddell Sea.

3.9. *Sensitivity to model parameters*

To determine the sensitivity of the model to various parameters, a series of simulations at a single location (38.40°W, 71.75°S) were performed. This location was chosen because sea ice persisted throughout the simula-
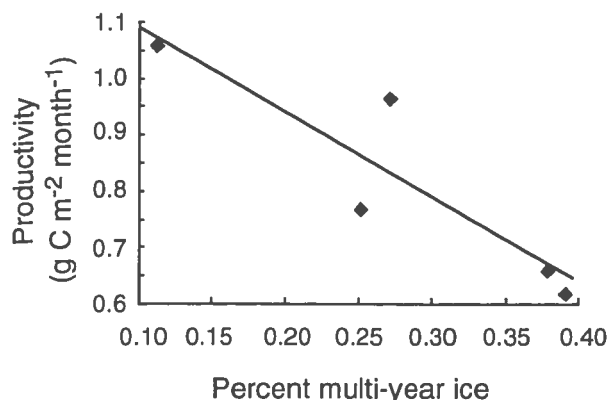
Fig. 8. The percent multi-year ice versus productivity per unit area of each geographic sector shown in Fig. 1, averaged over the duration of the simulation.

tion and biomass levels were moderate in magnitude. In these simulations, a single parameter was varied by ±50% while all others were held constant. The primary model inputs used in the sensitivity analysis, along with
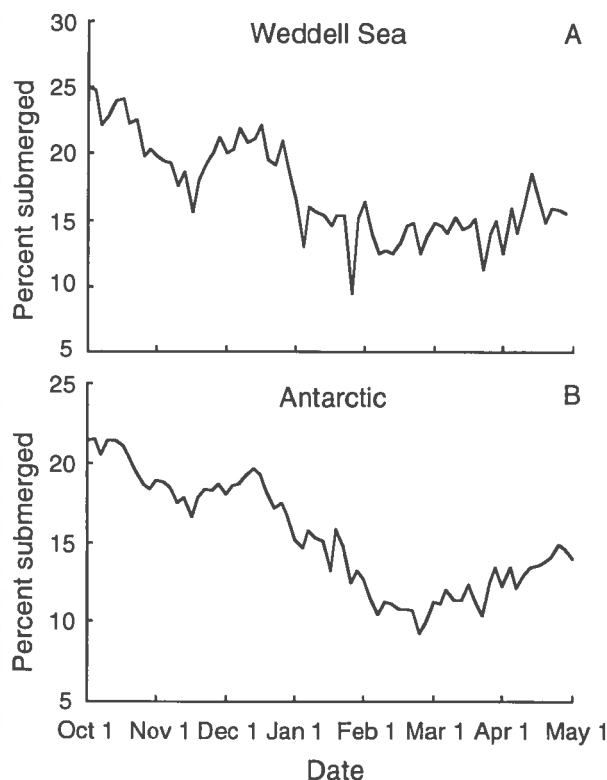

Fig. 9. Temporal changes in the percentage of sea ice area forced below the freeboard level due to snow loading for both the Weddell Sea and the entire Antarctic ice pack. The mean for the Weddell Sea (17.1%) is very close to the observed value of 17.4% [*Wadhams et al.*, 1987].

the rate of primary production computed using default coefficient values, are shown in Figure 10.

3.9.1 *Spectral photoadaptation parameter*.

Algal productivity in the model is controlled to a large degree by the value of I_k', which is scaled to simulate photoacclimation to changes in ambient irradiance (Figure 5C). The rationale is that under light limiting conditions, algae will modulate their spectrally corrected photosynthetic efficiency (α') and their carbon assimilation rate (P_m) such that I_k' ($=P_m/\alpha'$) is roughly equivalent to the average irradiance (PUR) experienced at a given depth. However, there appears to be an upper and lower limit to the extent to which I_k' will change as P_m and α' are adjusted, and field studies (Figure 5C) suggest that the maximum value of I_k' attained by sea ice algae ($I_{k'max}$) is approximately 20 µEin m^{-2} s^{-1}. Therefore, even if PUR exceeds 20 µEin m^{-2} s^{-1}, the level of I_k' expressed by an algal population will not. A intermediate light levels, I_k' will be approximately equal to PUR, and at extremely low light levels, I_k' will reach its lower limit, which is approximately equal to 10% of $I_{k'max}$.

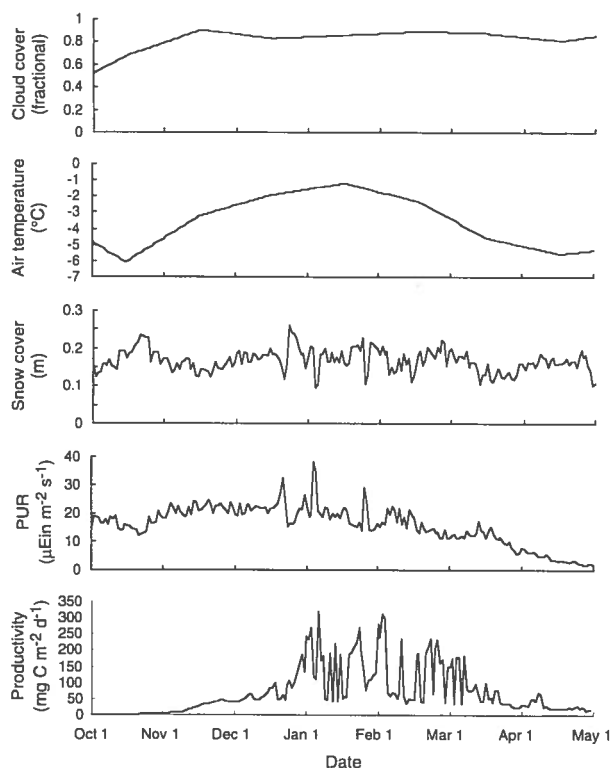Fortunately, the value for $I_{k'max}$ for sea ice algae has

Fig. 10. Temporal changes in the primary model inputs used in sensitivity analyses, along with the rate of primary production computed using the default coefficient values.
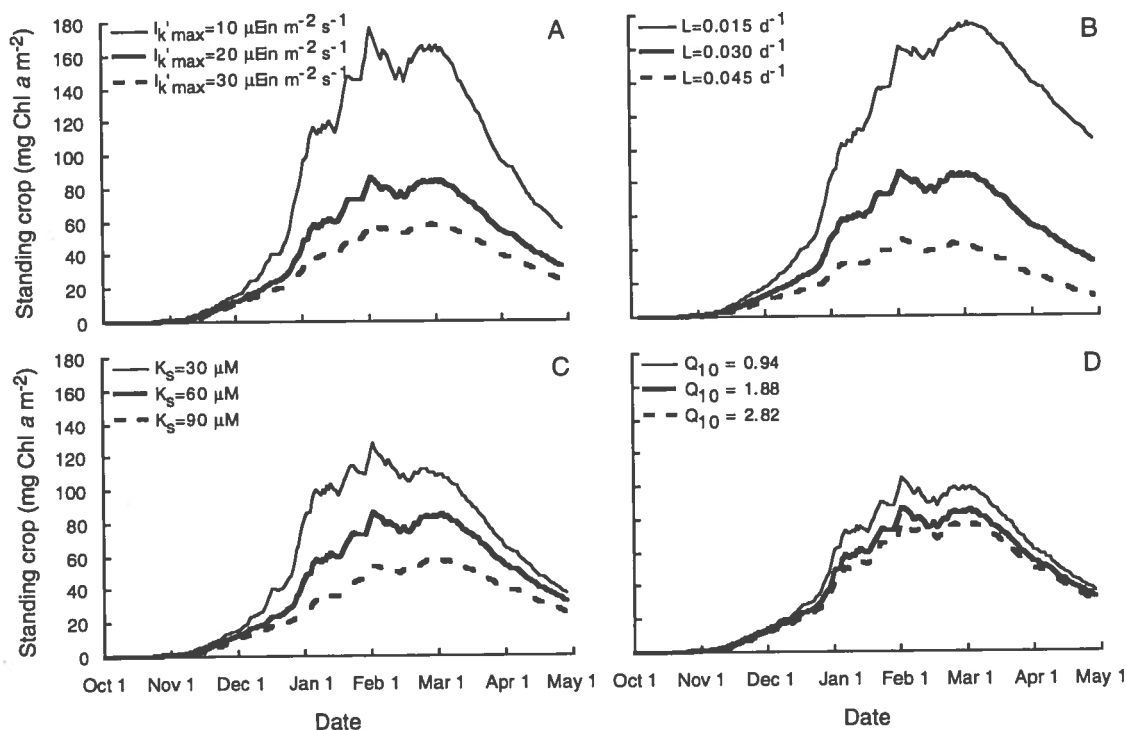
Fig. 11. Results of sensitivity analyses showing the effects of a 50% change in (*a*) $I_k'{}_{max}$, (*b*) L, the specific algal loss rate, (*c*) K_s for silicate, and (*d*) Q_{10}.

been reasonably well established [*Arrigo and Sullivan*, 1994] because the model is quite sensitive to this parameter (Figure 11A). Lowering the value of $I_k'{}_{max}$ in the model allows photosynthetic rates to saturate at lower irradiance and, if nutrients are in sufficient supply, increases algal growth rates. By late December, the microalgal standing crop was more than twice as great in the simulation where $I_k'{}_{max}$ was decreased to 10 μEin m^{-2} s^{-1} than when it was held at 20 μEin m^{-2} s^{-1}. An increase in $I_k'{}_{max}$ of 50% has a much less dramatic effect, resulting in approximately a 25% decline in algal biomass. The sensitivity of the model to $I_k'{}_{max}$ suggests that primary production in pack ice is determined primarily by both light availability and nutrient supply. When nutrient supply increases, either by surface flooding or infiltration through a porous ice pack, the nutrients cease to be the factor limiting algal growth. At this time, light level will determine algal growth rate. When nutrient supplies diminish, the importance of the light level is reduced because there are insufficient nutrients to support whatever level of algal growth the ambient light would have otherwise allowed. In fact, throughout most of the sensitivity analyses, light is available to some degree, although the availability varies dramatically depending upon time of year, atmospheric conditions, and snow cover. In

contrast, nutrients are often depleted completely in a particular region and growth cannot commence until they are resupplied.

3.9.2. Algal loss rate. The model is similarly sensitive to the algal specific loss rate, L, which combines death, grazing, and sinking into a single parameter. Ideally, these processes would be considered separately, but because of a lack of data, that is not possible at the present time. When L was low (0.015 d^{-1}), the rate of biomass accumulation increased during the first half of the simulation and the rate of decline after about March 1 was greatly reduced (Figure 11B). This resulted in estimates of algal standing crop which, by the end of April, were >300% too high. A 50% increase in L (0.045 d^{-1}) resulted in a 40% reduction in algal standing crop by early January which continued until the end of the simulation. The high sensitivity of the model to changes in L highlights the need for further investigation of the processes leading to the loss of algal biomass from the pack ice ecosystem.

The loss rates used in the model are low when compared to rates measured in other marine environments (0.10 d^{-1} or more). They also are low compared to field studies which suggest that microzooplankton in the Weddell Sea can graze sea ice algae with nearly 100%

efficiency [*Garrison and Buck*, 1991]. Because the loss rate used in the model was determined by adjusting its value until the simulated algal standing crop in the Weddell Sea was in agreement with in situ observations, there are only two explanations for its low value. Either the value is actually correct (or nearly so) or the algal growth rates estimated by the model are too low. It is doubtful that algal growth rates are seriously underestimated for a variety of reasons. At the location where the sensitivity analyses were conducted, algal biomass reached a peak of only 6 mg Chl *a* m^{-2} (300 mg C m^{-2}), hardly an exceptional value. Surprisingly, the rate of primary production at this location often exceeded 300 mg C m^{-2} d^{-1} (Figure 10), corresponding to a specific algal growth rate of approximately 0.7 d^{-1} during these high productivity events. This latter value is indeed high and near the maximum rate expected at the low temperatures characteristic of the sea ice. In addition, the surface area predicted by the model to be flooded at any given time (10-30% depending on location) agrees very well with in situ observations made in the Weddell Sea [*Wadhams et al.*, 1987], indicating that the model does not overly restrict nutrient supply. Furthermore, the model assumes that nutrients never become limiting so long as the surface is flooded (infiltration and freeboard communities) or the ice is sufficiently porous (the freeboard layer only).

Therefore, we believe that algal loss rates from the sea ice are low compared to losses measured in the water column, at least between November and April. We cannot rule out the possibility, however, that the loss rate may be time dependent and may increase through time as the sea ice degrades and zooplankton populations increase. The standing crop estimated by the model in April are about 20% higher than observations (Figure 6A), suggesting perhaps that the loss rate used by the model at this time is too low. However, only a small increase in L at the end of the simulation would bring monthly mean algal biomass levels into agreement with observations. While microzooplankton have been shown to be efficient grazers, it is clear that an efficiency of nearly 100% is not the norm since this would preclude any accumulation of algal biomass within the sea ice. Finally, it must be remembered that the loss rate of 0.03 d^{-1} used in the model represents an average over an area of approximately 625 km^2. In isolated locations within this area, the model could support loss rates much higher than this, so long as the mean remained 0.03 d^{-1}.

3.9.3. *Growth on and uptake of silicate*. Because little is presently known about the value K_s for silicate uptake in pack ice microalgae, information from similar microalgal populations was used to determine a reason-

able value for use in the model. C. Sullivan et al. (personal communication.), using ^{68}Ge(OH)$_4$ (an analog for silicic acid, *Azam et al.*, 1974), determined that the K_s value for sea ice microalgae collected from McMurdo Sound was >100 μM. Similarly, *Sommer* [1986] measured values of K_s for growth on silicate in the Antarctic diatoms *Corethron criophilum* and *Nitzschia kergulensis* of 60.1 and 88.7 μM, respectively, similar to the high values observed by C. Sullivan et al. (personal communication). *Jacques* [1983] measured levels of K_s for silicate uptake in Antarctic phytoplankton which were in excess of 30 μM. All of these values for Antarctic microalgae are significantly higher that the K_s measured by *Paasche* [1973a, 1973b] for temperate diatoms which ranged from 0.08 to 3.7 μM. Much more information about this parameter for sea ice microalgae is required before K_s can be further constrained.

Model results are less sensitive to changes (30-90 μM) in the half saturation constant (K_s) for silicate uptake (Figure 11C) than to changes in $I_k'_{max}$ or L, and not sensitive at all to changes in the K_s for nitrate uptake. These parameters control the degree of nutrient limitation according to the relationship illustrated in Eq. 8. The difference in the behavior of these two parameters exists because the K_s for silicate is generally high (60 μM) compared to the concentration of silicate in the environment, in contrast to the K_s for nitrate which is relatively small (0.5 μM). A 50% decrease in the K_s for silicate resulted in a 50% increase in algal standing crop; a 50% increase in K_s resulted in a drop in algal biomass of approximately 35%.

3.9.4. *Temperature*. It has been shown that algae often respond to changes in temperature according to the relationship given in Eq. 6. The values for G_o and r_G used in the model yield a Q_{10} of approximately 1.88, meaning that for a 10°C increase in temperature, algal growth rate will increase by a factor of 1.88. Raising the value of Q_{10} in the model heightens the sensitivity of algal growth to changes in temperature. Interestingly, the model was only slightly sensitive to a 50% change in Q_{10} (Fig 11D), varying by little more than 15%. This lack of sensitivity in the model is not so much due to the effect of the parameter itself, but rather the fact that temperature did not change by more than a few degrees during the peak growth period (December-January) during the simulation.

4. CONCLUSIONS

The results from the first large-scale application of a sea ice primary production model to the Southern Ocean

have been fruitful in a number of ways. First, we were able to reach approximate agreement with previous estimates of the magnitude of primary production [*Legendre et al.*, 1992] in these systems using a different approach, but with the same assumption that near-surface algal communities are responsible for most of the productivity. Because surface algal blooms will have an independent effect on the quantity and quality of light reaching internal or bottom ice algal communities, the model output from this study will be useful as an input for model runs to estimate the productivity of algae deeper in the ice column. Second, the formulation and successful use of this sea ice productivity model gives us a consistent framework for making comparisons with results from a similarly-formulated model for Southern Ocean phytoplankton that we have developed [*Arrigo et al.* in prep.]. Finally, the sensitivity analysis of the model has provided us with some guidance as to which parameters may be best to focus on for future field studies, such as the photosynthesis-irradiance relationships, loss rates and nutrient kinetics.

REFERENCES

Ackley, S. F., K. A. Buck, and S. Taguchi, Standing crop of algae in the sea ice of the Weddell Sea region, *Deep-Sea Res.*, *26*, 269-281, 1979.

Ackley, S. F., and C. W. Sullivan, Physical controls on the development and characteristics of Antarctic sea ice biological communities- a review and synthesis, *Deep-Sea Res.*, *41*, 1583-1604, 1994.

Arrigo, K. R., C. W. Sullivan, and J. N. Kremer, A bio-optical model of Antarctic sea ice, *J. Geophys. Res.*, *96*, 10581-10592, 1991.

Arrigo, K. R., and C. W. Sullivan, The influence of salinity and temperature covariation on the photophysiological characteristics of Antarctic sea ice microalgae, *J. Phycol.*, *28*, 746-756, 1992.

Arrigo, K. R., J. N. Kremer, and C. W. Sullivan, A simulated Antarctic fast-ice ecosystem, *J. Geophys. Res.*, *98*, 6929-6946, 1993a.

Arrigo, K. R., D. H. Robinson, and C. W. Sullivan, A high resolution study of the platelet ice ecosystem in McMurdo Sound, Antarctica: Photosynthetic and bio-optical characteristics of a dense microalgal bloom, *Mar. Ecol. Prog. Ser.*, *98*, 173-185, 1993b.

Arrigo, K. R., and C. W. Sullivan, A high resolution bio-optical model of microalgal growth: Tests using sea ice algal community time series data, *Limnol. Oceanogr.*, *39*, 609-631, 1994.

Arrigo, K. R., G. L. van Dijken, and J. C. Comiso, Estimating the Thickness of Sea Ice Snow Cover in the Weddell Sea from Passive Microwave Brightness Temperatures, *NASA Technical Memorandum 104640*, 1996.

Azam, F., B. B. Hemmingsen, and B. E. Volcani, Role of silicon in diatom metabolism. VI. Silicic acid transport and metabolism in the heterotrophic diatom *Nitzschia alba.*, *Arch. Mikrobiol.*, *97*, 103-114, 1974.

Blackman, F. F., Optima and limiting factors, *Ann. Bot.*, *19*, 281-295, 1905.

Bunt, J. S., Microalgae of the Antarctic pack ice zone, in *Symposium on Antarctic Oceanography*, edited by R. Currie, pp. 198-218, W. Heffner & Sons Ltd., Cambridge, UK., 1968.

Bunt, J. S., and C. C. Lee, Seasonal primary production in Antarctic sea ice at McMurdo Sound in 1967, *J. Mar. Res.*, *28*, 304-320, 1970.

Burkholder, P. R., and E. F. Mandelli, Productivity of microalgae in Antarctic sea ice, *Science*, *149*, 872-874, 1965.

Conkright, M. E., S. Levitus, and T. P. Boyer, *World Ocean Atlas 1994, Volume 1: Nutrients*, NOAA Atlas NESDIS 1, U. S. Department of Commerce, NOAA, NESDIS, 1994.

da Silva, A. M., C. C. Young and S. Levitus, *Atlas of Surface Marine Data 1994, Volume 1: Algorithms and procedures*, NOAA Atlas NESDIS 6, U. S. Department of Commerce, NOAA, NESDIS, 1994.

Eicken, H., M. A. Lange, H.-W. Hubberton, and P. Wadhams, Characteristics and distribution patterns of snow and meteoric ice in the Weddell Sea and their contribution to the mass balance of sea ice, *Ann. Geophysicae*, *12*, 80-93, 1994.

El Sayed, S. Z., Primary productivity and estimates of potential yields of the Southern Ocean, in Polar Research, edited by M. A. McWhinnie, pp. 141-160, Westview Press, New York., 1978.

Eppley, R. W., Temperature and phytoplankton growth in the sea, *Fish. Bull.*, *70*, 1063-1085, 1972.

Fogg, G. E., Aquatic primary production in the Antarctic, *Phil. Trans. R. Soc. Lond. B*, *279*, 27-38, 1977.

Fritsen, C. H., V. I. Lytle, S. F. Ackley, and C. W. Sullivan, Autumn bloom of Antarctic pack-ice algae, *Science*, *266*, 782-784, 1994.

Fritsen, C. H., S. F. Ackley, J. N. Kremer, and C. W. Sullivan, Flood-freeze cycles and microalgal dynamics in Antarctic pack ice, this volume.

Garrison, D. L., S. F. Ackley, and K. R. Buck, A physical mechanism for establishing algal populations in frazil ice, *Nature*, *306*, 363-365, 1983.

Garrison D. L., C. W. Sullivan, and S. F. Ackley, Sea ice microbial communities in Antarctica, *BioScience*, *36*, 243-250, 1986.

Garrison, D. L., A. R. Close, and E. Reimnitz, Algae concentrated by frazil ice: evidence from laboratory and field measurements, *Antarctic Science*, *1*, 313-316, 1990.

Garrison, D. L., and K. R. Buck, Surface-layer sea ice assemblages in Antarctic pack ice during the austral spring: environmental conditions, primary production and community structure, *Mar. Ecol. Prog. Ser.*, *75*, 161-172, 1981.

Grant, W. S., and R. A. Horner, Growth responses to salinity variation in four Arctic ice diatoms, *J. Phycol.*, *12*, 180-185, 1976.

Gregg, W. W. and K. L. Carder, A simple spectral solar irradiance model for cloudless maritime atmospheres, *Limnol. Oceanogr. 35*, 1657-1675, 1990.

Grossi, S. M., S. T. Kottmeier, and C. W. Sullivan, Sea ice microbial communities. III. Seasonal abundance of microalgae and associated bacteria, McMurdo Sound, Antarctica, *Microb. Ecol.*, *10*, 231-242, 1984.

Grossi, S. M., S. T. Kottmeier, R. L. Moe, G. T. Taylor, and C. W. Sullivan, Sea ice microbial communities. VI. Growth and primary production in bottom ice under graded snow cover, *Mar. Ecol. Prog. Ser.*, *35*, 153-164, 1987.

Holm-Hansen, O., S. Z. El Sayed, G. A. Franceschini, and R. Cuhel, Primary production and the factors controlling phytoplankton growth in the Southern Ocean, in *Adaptations within Antarctic ecosystems*, edited by G. A. Llano, Proc. Third SCAR Symp. on Antarctic Biology, pp. 11-50, Smithsonian Instit., Washington DC, 1977.

Jacques, G., Some ecophysiological aspects of the Antarctic phytoplankton, *Polar Biol.*, *2*, 27-33, 1983.

Kristianson, S., and E. E. Syvertsen, Sea ice algae in the Weddell Sea during austral spring 1988, (abstract), *Eos Trans. AGU*, *71*, 79, 1990.

Legendre, L., S. F. Ackley, G. S. Dieckmann, B. Gullicksen, R. Horner, T. Hoshiai, I. A. Melnikov, W. S. Reeburgh, M. Spindler, and C. W. Sullivan, Ecology of sea ice biota: 2. Global significance, *Polar Biol.*, *12*, 429-444, 1992.

Levitus, S., R. Burgett and T. P. Boyer, *World Ocean Atlas 1994, Volume 3: Salinity*, NOAA Atlas NESDIS 3, U. S. Department of Commerce, NOAA, NESDIS, 1994.

Lizotte, M. P., and C. W. Sullivan, Photosynthesis-irradiance relationships in microalgae associated with Antarctic pack ice: evidence for in situ activity, *Mar. Ecol. Prog. Ser.*, *71*, 175-184, 1991.

Lizotte, M. P., and C. W. Sullivan, Photosynthetic capacity in microalgae associated with Antarctic pack ice, *Polar Biol.*, *12*, 497-502, 1992.

Lizotte, M. P., and K. R. Arrigo, Modeling Irradiance in Pack Ice Floes (abstract), *Eos Trans. AGU, 73*(43), Fall Meeting Suppl., 290, 1992.

Mathot, S., D. L. Garrison, C. Lancelot, Pelagic and ice based primary production in the Southern Ocean (abstract), *Eos Trans. AGU, 76*(3), Ocean Sciences Suppl., OS143, 1996

Monod, J., Recherches sur la croissance des cultures bacteriennes, *Herman et Cie*, 1942.

Morel, A., Available, usable, and stored radiant energy in relation to marine photosynthesis. *Deep-Sea Res.*, *25*, 673-688, 1978.

Paasche, E., Silicon and the ecology of marine plankton diatoms. I. *Thalassiosira pseudonana* grown in a chemostat with silicate as limiting nutrient, *Mar. Biol.*, *19*, 117-126, 1973a.

Paasche, E., Silicon and the ecology of marine plankton diatoms. II. Silicate uptake kinetics in five diatom species, *Mar. Biol.*, *19*, 262-269, 1973b.

Palmisano A. C., and C. W. Sullivan, Sea ice microbial communities (SIMCO). I. Distribution, abundance, and primary production of ice microalgae in McMurdo Sound, Antarctica in 1980, *Polar Biol.*, *2*, 171-177, 1983.

Palmisano, A. C., J. B. SooHoo, and C. W. Sullivan, Effects of four environmental variables on photosynthesis-irradiance relationships in Antarctic sea-ice microalgae, *Mar. Biol.*, *94*, 299-306, 1987.

Priscu, J. C, and C. W. Sullivan, Nitrogen metabolism in Antarctic fast-ice microalgal assemblages, this volume.

Robinson, D. H., Photosynthesis in sea ice microalgae: Response to low temperatures and extremes of irradiance, Ph.D. thesis, Univ. Southern California, Los Angeles, 1992.

Ryther, J. H., Geographic variations in productivity, in *The Sea Vol. 1*, edited by M. N. Hill, , pp. 347-380, Interscience Publ., New York, 1963.

Smetacek, V., R. Scharek, E. M. Nöthig, Seasonal and regional variation in the palagial and its relationship to the life history cycle of krill, in *Antarctic ecosystems- ecological change and conservation*, edited by K. R. Kerry and G. Hempel, pp. 103-114, Springer, Berlin, Heidelberg, New York, 1990.

Smetacek, V., R. Scharek, L. I. Gordon, H. Eicken, E. Fuhrbach, G. Rohardt, and S. Moore, Early spring phytoplankton blooms in ice platelet layers of the southern Weddell Sea, Antarctica, *Deep-Sea Res.*, *38*, 153-168, 1992.

Smith, W. O., and Nelson, D. M., The importance of ice-edge phytoplankton blooms in the Southern Ocean, *BioScience*, *36*, 251-257, 1986.

Sommer, U., Nitrate and silicate-competition among Antarctic phytoplankton, *Mar. Biol. 91*, 345-351, 1986.

Spies, A., Growth rates of Antarctic marine phytoplankton in the Weddell Sea, *Mar. Ecol. Prog. Ser.*, *41*, 267-274, 1987.

Wadhams, P., M. A. Lange and S. F. Ackley, The ice thickness distribution across the Atlantic sector of the Antarctic Ocean in midwinter, *J. Geophys. Res. 92*, 14,535-14,552, 1987.

Zwally, H. J., C. Parkinson, F. Carsey, P. Gloersen, W. J. Campbell, and R. O. Ramseier, Antarctic sea ice variations 1973-1975, *NASA Weather Clim. Rev. Pap.*, *56*, 335-340, 1979.

K. R. Arrigo, NASA Goddard Space Flight Center, Oceans and Ice Branch, Code 971.0, Greenbelt, MD 20771.

D. L. Worthen, Science Systems and Applications, Inc., Lanham, MD 20706.

P. Dixon, Scripps Institution of Oceanography, University of California, San Diego, La Jolla, CA 92093.

M. P. Lizotte, Department of Biology and Microbiology, University of Wisconsin, Oshkosh, Oshkosh, WI, 54901-8640.